**DOE Grant DE-SC0008639**

# Influence of Multi-Valency, Electrostatics and Molecular Recognition on the Adsorption of Transition Metal Complexes on Metal Oxides: A Molecular Approach to Catalyst Synthesis

Robert M. Rioux
Department of Chemical Engineering and Department of Chemistry
Pennsylvania State University
University Park, PA 16802-4400
rioux@engr.psu.edu

## Executive Summary (DE-FG02-12ER16364)

In this work, we have primarily utilized isothermal titration calorimetry (ITC) and complimentary catalyst characterization techniques to study and assess the impact of solution conditions (i.e., solid-liquid) interface on the synthesis of heterogeneous and electro-catalysts. Isothermal titration calorimetry is well-known technique from biochemistry/physics, but has been applied to a far lesser extent to characterize buried solid-liquid interfaces in materials science. We demonstrate the utility and unique information provided by ITC for two distinct catalytic systems. We explored the thermodynamics associated catalyst synthesis for two systems: (*i*) ion-exchange or strong electrostatic adsorption for Pt and Pd salts on silica and alumina materials (*ii*) adsorption to provide covalent attachment of metal and metal-oxo clusters to Dion-Jacobsen perovskite materials.

Our work has been published in the Journal of the American Chemical Society (2), Nature Chemistry (1), Journal of Catalysis (1), Green Chemistry (1), Physical Chemistry Chemical Physics (1), Journal of Physical Chemistry (1), Catalysis Science and Technology (1) and ACS Catalysis (2). We currently have papers under review or re-review in Nature Chemistry and the Journal of Physical Chemistry C. We have a number of papers under preparation/revision for submission to the Journal of Catalysis.

1. C. S. Spanjers, P. Guillo, T. D. Tilley, M. J. Janik, R. M. Rioux. Identification of Second Shell Coordination in Transition Metal Species Using Theoretical XANES: Example of Ti-O-(C, Si, Ge) Complexes. *J. Phys. Chem. A* **121** (2017) 162-167. DOI: 10.1021/acs.jpca.6b12197
2. J. Saavedra, T. Whittaker, Z. F. Chen, C. J. Pursell, R. M. Rioux, B. D. Chandler. Controlling activity and selectivity using water in the Au-catalysed preferential oxidation of CO in $H_2$. *Nature Chemistry* **8** (2016) 585-590. DOI: 10.1038/NCHEM.2494
3. M. E. Strayer, T. P. Senftle, J. P. Winterstein, N. M. Vargas-Barbosa, R. Sharma, R. M. Rioux, M. J. Janik, T. E. Mallouk. Charge Transfer Stabilization of Late Transition Metal Oxide Nanoparticles on a Layered Niobate Support. *J. Am. Chem. Soc*. **137** (2015) 16216-16224. DOI: 10.1021/jacs.5b11230
4. B. Panthi, A. Mukhopadhyay, L. Tibbits, J. Saavedra, C. J. Pursell, R. M. Rioux, B. D. Chandler. Using Thiol Adsorption on Supported Au Nanoparticle Catalysts to Evaluate Au Dispersion and the Number of Active Sites for Benzyl Alcohol Oxidation. *ACS Catal*. **5** (2015) 2232-2241. DOI: 10.1021/cs501942t
5. D. J. Childers, N. M. Schweitzer, S. M. K. Shahari, R. M. Rioux, J. T. Miller, R. J. Meyer. Modifying structure-sensitive reactions by addition of Zn to Pd. *J. Catal.* **318** (2014) 75-84. DOI: 10.1016/j.jcat.2014.07.016.

6. M. E. Strayer, J. M. Binz, M. Tanase, S. M. K. Shahri, R. Sharma, R. M. Rioux, T. E. Mallouk. Interfacial Bonding Stabilizes Rhodium and Rhodium Oxide Nanoparticles on Layered Nb Oxide and Ta Oxide Supports. *J. Am. Chem. Soc*. **136** (2014) 5687-5696. DOI: 10.1021/ja412933k
7. M. A. Smith, A. Zoelle, Y. Yang, R. M. Rioux, N. G. Hamilton, K. Arnakawa, P. K. Nielsen, A. Trunschke. Surface roughness effects in the catalytic behavior of vanadia supported on SBA-15. *J. Catal.* **312** (2014) 170-178. DOI: 10.1016/j.jcat.2014.01.011.
8. C. S. Spanjers, T. P. Senftle, A. C. T. van Duin, M. J. Janik, A. I. Frenkel, R. M. Rioux. Illuminating surface atoms in nanoclusters by differential X-ray absorption spectroscopy. *Phys. Chem. Chem. Phys*. **48** (2014) 26528-26538. DOI: 10.1039/c4cp02146k.
9. D. J. Childers, N. M. Schweitzer, S. M. K. Shahri, R. M. Rioux, J. T. Miller, R. J. Meyer. Evidence for geometric effects in neopentane conversion on PdAu catalysts. *Catal. Sci. Technol*. **4** (2014) 4366-4377. DOI: 10.1039/c4cy00846d
10. Y. Yang, R. M. Rioux. Highly stereoselective anti-Markovnikov hydrothiolation of alkynes and electron-deficient alkenes by a supported Cu-NHC complex. *Green Chem.* **16** (2014) 3916-3925. DOI: 10.1039/c4gc00642a

## Interfacial bonding stabilizes rhodium and rhodium oxide nanoparticles on layered Nb- and Ta-oxide supports

The metal/oxide interface is vital to many current and developing technologies, including nanoscale electronic contacts, biomedical implants and sensors, fuel cell catalysis, photocatalysis, and heterogeneous catalysis.[1-5] Many heterogeneous catalysts consist of late transition metal nanoparticles supported on high surface area oxides, and these particles can coarsen under catalytic reaction conditions. The coarsening presents lifetime and regeneration issues for reactions such as CO oxidation using Cu and Ag catalysts,[6,7] selective oxidation of alcohols on supported Ag catalysts,[8] and water-gas shift and methanol synthesis reactions with supported Cu or Fe nanoparticles.[9] Oxide-supported Rh, Ni, Pd, and Pt catalysts are also prone to coarsening at higher temperatures.[2,3,10]Much effort has been devoted to inhibiting the growth of metal particles in these catalytic systems. One way nanoparticle catalyst growth can be limited is to disperse the nanoparticles in a porous network, such as a zeolite or high surface area oxide support.[11] In a recent example, gold nanoparticles were stabilized by physically segregating them between sheets of alumina with rough surfaces.[12]

Chemically specific interactions between metal nanoparticles and oxide supports are also well known to stabilize metal nanoparticle catalysts. The strong metal-support interaction (SMSI) refers to the stabilization of late transition metals - Rh, Au, Pd, and Pt - by certain oxide supports. The SMSI was first described by Tauster and Fung in the late 1970's[13-15] and refers to the physical covering, or encapsulation, of late transition metal particles by a metal oxide.[16-22] This process is thought to be driven by local reduction of the oxide and thus requires a reducible metal oxide such as $TiO_2$ or $Nb_2O_5$. Both electron microscopy data and the observation that $H_2$ and CO chemisorption are suppressed on supported metal nanoparticles are consistent with this encapsulation model. The SMSI has been correlated with differences in surface energies and work functions between the late transition metal and the early transition metal oxide, and this is consistent with the reduction model;[19] however, recent SMSI observations with Au/ZnO do not fit this trend.[23]

Local, covalent bonding at the metal/oxide interface can also stabilize supported metal or metal oxide nanoparticles in the absence of encapsulation by the support. Recently, Campbell has described the electronic metal-support interaction (EMSI), which involves both electronic and geometric interactions between a nanoparticle and support.[24] Electronic structure calculations by Jarvis and Carter have pointed out the importance of covalent bonding through d-electron interactions in stabilizing the adhesion of late transition metals to early transition metal oxides.[25] These d-electron acid-base effects are reminiscent of earlier observations of the anomalous stability of early-late transition metal alloys such as $ZrPt_3$.[26,27] Our group recently discovered anomalous stabilization of rhodium hydroxide/oxide nanoparticles deposited on sheets of the layered oxides $KCa_2Nb_3O_{10}$[4] and $K_4Nb_6O_{17}$.[28] In these studies, 1 nm to 2 nm nanoparticles remained well dispersed on the nanosheets when heated in air to 350 °C, despite the fact that Rh was not reduced to the metal.

To date, there have been limited experimental data that can directly quantify the strengths of covalent nanoparticle-support interactions. Recently, Campbell and coworkers used microcalorimetry to directly interrogate the bonding between metal atoms and clean, crystallographically well-defined oxide surfaces in ultrahigh vacuum (UHV). Using this technique, they found evidence of strong interfacial bonding between Au nanoparticles and $CeO_2$.[29,30] In this paper we report the use of isothermal titration calorimetry (ITC)[31,32] to measure directly the enthalpy of interaction between rhodium hydroxide nanoparticles and metal oxides under wet chemical synthetic conditions. Unilamellar metal oxide nanosheets, prepared by exfoliation of layered oxides and metal phosphates, were used as supports in order to enable imaging of the supported nanoparticles by high-resolution transmission electron microscopy (HRTEM). The compositional variety

of these nanosheets allows us to compare the behavior of reducible and non-reducible metal oxides, and the behavior of transition metal oxide supports to that of layered silicates and metal phosphates. HRTEM, X-ray absorption, and x-ray scattering methods were used to study the evolution of particle size and interfacial bonding as a function of temperature under both oxidizing and reducing atmospheres. These studies establish a clear connection between the strength of interfacial bonding and the chemical behavior of supported rhodium hydroxide/oxide nanoparticles.

## Results and Discussion

The phase purity of $KCa_2Nb_3O_{10}$,[33] $K_4Nb_6O_{17}$,[34,35] $RbTaO_3$[36] and α-ZrP[37] was confirmed by comparing powder XRD patterns with literature reports. The layered oxides $KCa_2Nb_3O_{10}$, $K_4Nb_6O_{17}$, and $RbTaO_3$ were acid-exchanged to yield $HCa_2Nb_3O_{10}\cdot 0.5H_2O$,[38] $K_{1.1}H_{2.9}Nb_6O_{17}\cdot nH_2O$[28] and $Rb_{0.1}H_{0.9}TaO_3\cdot 1.3H_2O$[36] and the phase purity was again established by XRD (Supporting Information, Figure S1). These samples were then exfoliated to give nanosheets of $TBA_{0.24}H_{0.76}Ca_2Nb_3O_{10}$, $TBA_{0.7}H_{2.2}K_{1.1}Nb_6O_{17}$, and $TBA_{0.1}H_{0.8}Rb_{0.1}TaO_3$ in excess $TBA^+OH^-$ solution. The stoichiometry of the exfoliated samples was obtained by titrating the residual basic solution after nanosheet exfoliation. From this back-titration, the amount of free base, and hence the amount of $TBA^+$ removed from solution by association with the nanosheets, was determined. The exfoliation of α-ZrP has been described in detail previously.[37] Na-TSM was exfoliated by addition to water to produce micron-sized sheets.[39]

$Rh(OH)_3$ nanoparticles were deposited on oxide supports by adding an aqueous solution of $RhCl_3\cdot 3H_2O$ to a suspension of nanosheets in excess $TBA^+OH^-$. The mass fraction of $Rh(OH)_3$ deposited is always 0.05 unless otherwise stated. Previous studies have established that this procedure gives < 1 nm diameter rhodium hydroxide nanoparticles on both $KCa_2Nb_3O_{10}$ and $K_4Nb_6O_{17}$ supports.[4,28] As previously reported, XRD patterns of these materials show only 00*l* and *hk*0 reflections after turbostratic restacking of the layered oxide and an increase in d-spacing as the loading of $Rh(OH)_3$ increases. As a control experiment, aqueous $RhCl_3\cdot 3H_2O$ solution was added to excess $TBA^+OH^-$ and the time course of hydrolysis and particle growth was measured by TEM. As seen in Figure 1A-B, the lateral dimensions of $Rh(OH)_3$ particles were (11 ± 3) nm after 1 min and grew to > 1 μm after 10 min. These results suggest that when the hydrolysis occurs in the $TBA_{0.24}H_{0.76}Ca_2Nb_3O_{10}$ and $TBA_{0.7}H_{2.2}K_{1.1}Nb_6O_{17}$ suspensions, the initially formed approximately 1 μm $Rh(OH)_3$ particles undergo "reverse" ripening to become well dispersed, < 1 nm nanoparticles. This hypothesis was verified by starting with independently-synthesized micron-size $Rh(OH)_3$ particles, which were added to a basic solution of $TBA_{0.24}H_{0.76}Ca_2Nb_3O_{10}$ to yield well-dispersed oxide-supported nanoparticles (Figure 1C). The breakup or dissolution of the larger $Rh(OH)_3$ particles appears to be driven thermodynamically by a favorable interaction between the nanoparticles and the support, which compensates for the increased surface energy of the nanoparticles. Complete deposition of rhodium hydroxide onto $TBA_{0.24}H_{0.76}Ca_2Nb_3O_{10}$ and $TBA_{0.7}H_{2.2}K_{1.1}Nb_6O_{17}$ was confirmed by both the formation of a clear solution, as $Rh(OH)_3$ is yellow in solution and ICP-AES, which confirmed that a mass fraction of 0.05 rhodium hydroxide was deposited onto the sample. In contrast, incomplete deposition of $Rh(OH)_3$ on the layered silicate Na-TSM was evidenced by the yellow color of the supernatant solution after centrifugation of the layered silicate, as well by the presence of high contrast, micron-size crystals with hexagonal texture (resembling those shown in Figure 1B) in the TEM analysis of the Na-TSM precipitate.

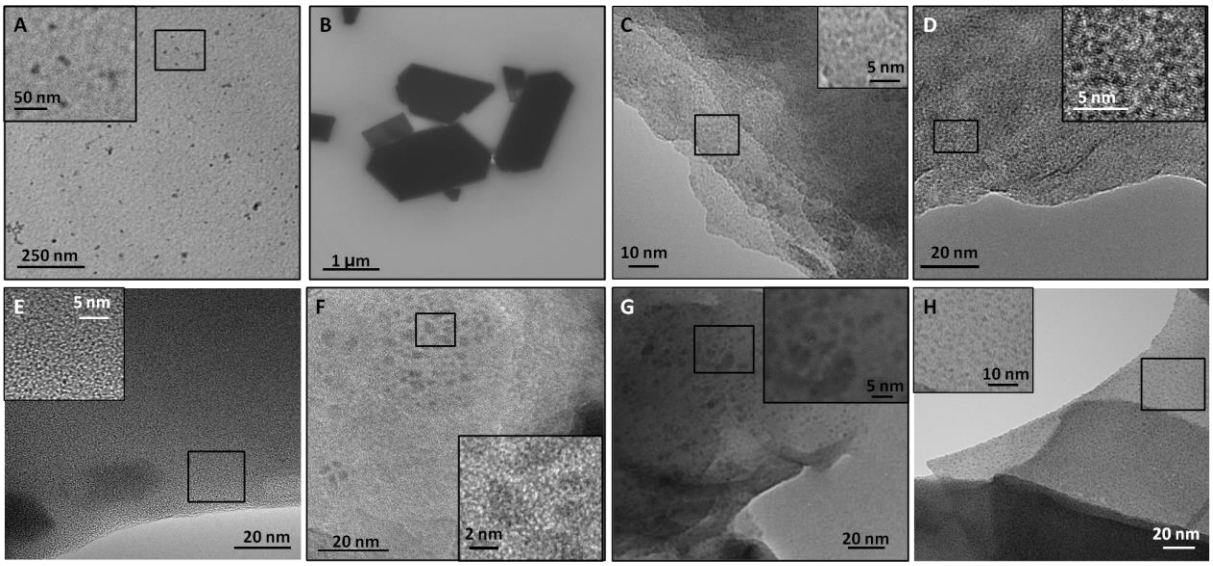


**Figure 1**. TEM images of $RhCl_3 \cdot 3H_2O$ in 25 mmol·L$^{-1}$ $TBA^+OH^-$ after (A) 1 min and (B) 10 min. (C) shows the "reverse" ripening of larger $Rh(OH)_3$ particles deposited onto $TBA_{0.24}H_{0.76}Ca_2Nb_3O_{10}$ to give highly dispersed nanoparticles. TEM images of $Rh(OH)_3$ deposited on $KCa_2Nb_3O_{10}$ (D), $K_4Nb_6O_{17}$ (E), Na-TSM (F), α-ZrP (G) and $HTaO_3$ (H) at ambient temperature.

Zeta-potential measurements show that the nanosheet suspensions of the oxide supports $KCa_2Nb_3O_{10}$ and $K_4Nb_6O_{17}$, as well as the $Rh(OH)_3$ particles, are negatively charged at the pH of the reaction.[4] Thus, a simple electrostatic interaction between the nanoparticles and niobate sheets cannot explain the small size and even distribution of nanoparticles on $KCa_2Nb_3O_{10}$ and $K_4Nb_6O_{17}$ supports (Figure 1D-E). In contrast, an uneven distribution of rhodium hydroxide nanoparticles was found on the Na-TSM and α-ZrP supports, with many areas not having any particles (Figure 1F-G). In both cases, a colored solution remained after rhodium hydroxide deposition and centrifugation, meaning that not all the rhodium hydroxide deposited onto the support. Because the SMSI mechanism is thought to involve local reduction of metal ions in the supporting oxide, [14,17-19,30,40-42] an additional experiment was performed with $TBA_{0.1}H_{0.8}Rb_{0.1}TaO_3$ nanosheets in place of layered niobates. Despite the fact that Ta(V) is much more difficult to reduce than Nb(V), the resulting materials - prepared under aerobic conditions - showed a uniform distribution of nanoscale particles ($1.3 \pm 0.3$) nm, $n = 101$, Figure 1H). The tantalate nanosheets are also negatively charged at the pH of the reaction (pH = 12.0). These data are consistent with the idea that the stabilization of $Rh(OH)_3$ nanoparticles arises from a specific chemical interaction with the support that is not driven by electrostatic interactions or local reduction.

Isothermal titration calorimetry (ITC) was used to investigate the strength of bonding between rhodium hydroxide nanoparticles and oxide supports. During a deposition reaction, several reactions occur simultaneously, and the overall process can be represented by the Born-Haber cycle shown in Scheme 1. The enthalpy associated with the interaction of the $Rh(OH)_3$ nanoparticles and the oxide support (Reaction 3) is determined by taking the difference between the overall reaction (Reaction 4) and the heats of hydrolysis (Reaction 1, $\Delta H_1 = (-27 \pm 5)$ kJ·mol$^{-1}$) and neutralization (Reaction 2, $\Delta H_2 = (-58 \pm 2)$ kJ·mol$^{-1}$). In this cycle, there is also a surface energy term that is dependent on the size of the particles produced. In order to obtain a reliable comparison of bonding energies for different supports, the final sizes of the $Rh(OH)_3$ nanoparticles should be similar. $Rh(OH)_3$ particles deposited on Na-TSM ($(5 \pm 1)$ nm, $n = 101$) are significantly larger than those deposited on Nb oxide nanosheets (< 1 nm diameter).

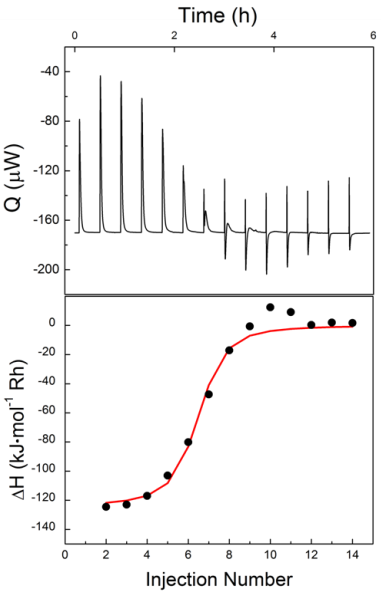


**Figure 2**. A) Real-time ITC thermogram for the addition of $RhCl_3$ aqueous solution to $TBA_{0.24}H_{0.76}Ca_2Nb_3O_{10}$ sheets in excess $TBA^+OH^-$ solution and B) the integrated heat data with an independent model fit.

Therefore, high surface area $SiO_2$ and γ-$Al_2O_3$ were used as non-transition metal oxide supports in the ITC experiments, as they gave $Rh(OH)_3$ nanoparticle sizes of $(0.7 \pm 0.2)$ nm ($n = 100$) and $(1.3 \pm 0.4)$ nm ($n = 100$), respectively. (Supporting Information, Figure S3). The γ-$Al_2O_3$ used in these experiments had an average particle diameter of $(50 \pm 40)$ nm ($n = 127$) and a surface area of $(35.8 \pm 0.1)$ m$^2$·g$^{-1}$. The $SiO_2$ support had an average particle diameter of $(17 \pm 6)$ nm ($n = 101$) and a surface area of $(408 \pm 8)$ m$^2$·g$^{-1}$. Both of these high surface area oxides are used widely as supports for rhodium and platinum nanoparticles. In addition, nanoparticles deposited on these supports are known to coalesce at temperatures as low at 550 °C.[2,43-45]

A representative ITC isotherm for $Rh(OH)_3$ deposition onto $TBA_{0.24}H_{0.76}Ca_2Nb_3O_{10}$ sheets and the associated integrated area plot are shown in Figure 2 and the heats of $Rh(OH)_3$ adsorbing to various oxide supports are listed in Table 1. The adsorption of $Rh(OH)_3$ to $TBA_{0.24}H_{0.76}Ca_2Nb_3O_{10}$, $TBA_{0.7}H_{2.2}K_{1.1}Nb_6O_{17}$, and $TBA_{0.1}H_{0.8}Rb_{0.1}TaO_3$ is exothermic, with $\Delta H_3$ values in the range of -32 kJ·mol$^{-1}$ Rh to -37 kJ·mol$^{-1}$ Rh. These three layered oxides are structurally different: $KCa_2Nb_3O_{10}$ contains only corner-sharing $NbO_6$ octahedra, whereas the corrugated sheets of $K_4Nb_6O_{17}$ and $RbTaO_3$ contain both edge and corner-shared octahedra. Nevertheless the $\Delta H_3$ values are all exothermic and quite similar. In contrast, $\Delta H_3$ values obtained with $SiO_2$ and γ-$Al_2O_3$ were both endothermic, $(25 \pm 6)$ kJ·mol$^{-1}$ and $(55 \pm 6)$ kJ·mol$^{-1}$, respectively. These differences are consistent with a relatively strong covalent interaction between $Rh(OH)_3$ and the layered niobate and tantalate supports. The difference in $\Delta H_3$ between $SiO_2$ and γ-$Al_2O_3$ may, in part, reflect a difference in the electrostatic energy of bringing negatively charged $Rh(OH)_3$ particles to the surfaces of these supports. $SiO_2$ and γ-$Al_2O_3$ have zeta-potentials of $(-37 \pm 1)$ mV and $(-44 \pm 1)$ mV, respectively. The less negative zeta-potential of $SiO_2$ results in less electrostatic repulsion and therefore, a smaller endothermic heat of interaction than with γ-$Al_2O_3$.

**Table 1**. Thermochemical data from ITC experiments for $Rh(OH)_3$ deposition onto metal oxide supports ($\Delta H_3$). The errors are reported as one standard deviation of the mean for triplicate measurements.

| Oxide support | $\Delta H_3$ (kJ·mol$^{-1}$) |
|---|---|
| $TBA_{0.24}H_{0.76}Ca_2Nb_3O_{10}$ | -35 ± 9 |
| $TBA_{0.7}H_{2.2}K_{1.1}Nb_6O_{17}$ | -37 ± 9 |
| $TBA_{0.1}H_{0.8}Rb_{0.1}TaO_3$ | -32 ± 10 |
| $\gamma$-$Al_2O_3$ | 55 ± 6 |
| $SiO_2$ | 25 ± 6 |

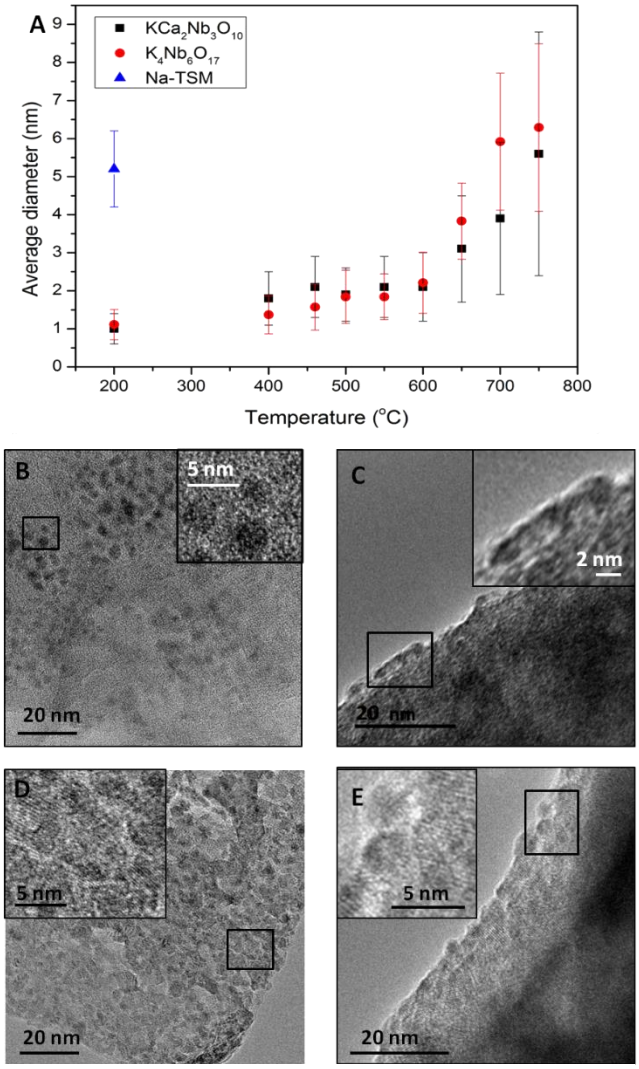


**Figure 3**. A) Plot of the average diameter of rhodium hydroxide/oxide nanoparticles with increasing temperature on $KCa_2Nb_3O_{10}$, $K_4Nb_6O_{17}$ and Na-TSM supports. The uncertainty reported for each measured value is one standard deviation of the mean for *n* measurements. See Supporting Information, Table S1 for number of measurements for each value. TEM images showing B) the uneven distribution of nanoparticles at 200 °C on Na-TSM; C) rhodium oxide nanoparticles on $K_4Nb_6O_{17}$ at 500 °C that begin to neck together; and the distribution of $Rh_2O_3$ particles on D) $KCa_2Nb_3O_{10}$ E) $K_4Nb_6O_{17}$ at 600 °C.

*In situ* TEM was performed to monitor the size evolution of $Rh(OH)_3$ nanoparticles as a function of temperature in vacuum. By statistically analyzing the particle size, the growth of nanoparticles was correlated with data from other physical characterization methods (see below) to identify the chemical changes that occurred upon heating. Three different supports were used in these experiments: two layered niobates ($KCa_2Nb_3O_{10}$ and $K_4Nb_6O_{17}$) and one (Na-TSM) that was chemically similar to the high surface area silica and alumina supports and did not show evidence of strong covalent bonding to $Rh(OH)_3$ in the ITC experiments. Figure 3A shows a plot of average $Rh(OH)_3/Rh_2O_3$ nanoparticle diameter versus temperature for samples that were heated in vacuum in the TEM. Average particle sizes are not shown for temperatures below 200 °C for the niobate supports because the nanoparticles were too small to obtain reliable size information. At 200 °C, both the $KCa_2Nb_3O_{10}$ and $K_4Nb_6O_{17}$ supports have evenly distributed nanoparticles with average diameters of (1.0 ± 0.4) nm and (1.1 ± 0.4) nm, respectively. The average diameter of nanoparticles deposited on Na-TSM at 200 °C is (5 ± 1) nm, and the particles are unevenly distributed on the support; i.e. there are some areas that have no nanoparticles present (Figure 3B). At temperatures above 200 °C, it is difficult to obtain statistical size information for nanoparticles deposited on Na-TSM because of the uneven distribution of larger particles. A TEM image of $Rh_2O_3$ nanoparticles on Na-TSM at 440 °C shows these larger particles.

As the temperature increases, nanoparticles on the niobate supports become visible in the TEM images, but are still less than 2 nm in diameter. At 400 °C, crystallization and faceting of the nanoparticles was noticeable. This is tentatively attributed to the phase change from $Rh(OH)_3$ to $Rh_2O_3$, but no lattice spacing corresponding to crystals of the latter could be found at this temperature.

Although the average diameters of the nanoparticles remained similar up to 600 °C, necking of the nanoparticles deposited on $K_4Nb_6O_{17}$ began at 500 °C, as shown in Figure 3C. This necking allows for diffusion of rhodium atoms between particles. At 500 °C, a change in the crystalline support is seen in both XRD and TEM. While the support is changing, the nanoparticle size remains constant, which again supports the idea that the nanoparticles are covalently anchored to the niobate sheets.Figure 3D-E shows the dispersion of approximately 2 nm diameter nanoparticles on $KCa_2Nb_3O_{10}$ and $K_4Nb_6O_{17}$ at 600 °C. At 650 °C, the average diameter of nanoparticles on both $KCa_2Nb_3O_{10}$ and $K_4Nb_6O_{17}$ begins to increase. The three nanoparticles that were necking together at 500 °C (Figure 3C) have coalesced into one larger particle at 650 °C. By 725 °C, hexagonal particles become obvious, which is indicative of corundum-structure $Rh_2O_3$ at this temperature. The particles were confirmed to be crystalline $Rh_2O_3$ at 750 °C (Supporting Information, Figure S5).[46] TEM statistical analysis shows that $Rh_2O_3$ nanoparticles grow at the same rate on $KCa_2Nb_3O_{10}$ and $K_4Nb_6O_{17}$. In contrast, the original distribution and growth of nanoparticles is drastically different on Na-TSM.

Rh metal nanoparticles on oxide supports are used widely in catalysis, and the temperature at which they can be used under reducing conditions is limited by their stability against growth. Therefore, *in situ* TEM was used to investigate the growth of Rh nanoparticles on both Nb oxide nanosheets and Na-TSM under reducing conditions. Figure 4A shows a plot of average nanoparticle diameter versus temperature for samples heated in hydrogen. The nanoparticles were too small to retrieve size information when deposited on $KCa_2Nb_3O_{10}$ and imaged at temperatures up to 200 °C. The nanoparticles deposited on $K_4Nb_6O_{17}$ were (0.5 ± 0.2) nm in diameter at 200 °C when heated in 200 Pa of hydrogen, compared to (1.1 ± 0.4) nm when heated in vacuum ($1 \times 10^{-6}$ Pa). When samples were heated in $H_2$, the growth of the nanoparticles was retarded for all supports relative to samples heated in vacuum (Figures 4B-E). Interestingly, nanoparticles deposited on $KCa_2Nb_3O_{10}$ and $K_4Nb_6O_{17}$ remain smaller than 2 nm diameter up to 700 °C. Since the

nanoparticles do not aggregate, they retain active surface area at increased temperatures, and thus niobates are likely to stabilize Rh nanoparticles under catalytic conditions.

Nanoparticles deposited on Na-TSM also remain small ((3.6 ± 0.9) nm) at 600 °C but they are not evenly dispersed. Below 600 °C, the particles are present only at the sheet edges (Figure 4D). At 600 °C, the nanoparticles move from the edges onto basal planes of the sheets (Figure 4E). This behavior differs from the other supports heated in $H_2$, where the nanoparticles were less than 2 nm and evenly distributed at all temperatures studied. $Rh(OH)_3$ nanoparticles deposited on Na-TSM and heated under vacuum also behaved differently. Under vacuum, the nanoparticles were unevenly distributed but did not segregate to the edges of the sheets. The $Rh_2O_3$ nanoparticles also grew rapidly with temperature under vacuum conditions.

Possible beam effects were investigated to confirm that the increase in particle size was due to the intended increase in temperature and not due to irradiation. An area of the support $K_4Nb_6O_{17}$ with deposited nanoparticles was bombarded with the electron beam for 12 min at 550 °C (electron density of $3\times10^7$ $e^-\cdot nm^{-1}$), which is the approximate length of time spent at each temperature during TEM imaging. During this time, no nanoparticle growth was evident. This leads to the conclusion that beam effects did not induce significant changes in nanoparticle size. Short timescale studies were also done *in situ* in the TEM to determine if kinetics played a role in the growth of the nanoparticles. During a typical TEM analysis, stabilization at a given temperature took up to 30 min. Samples with nanoparticles deposited on $KCa_2Nb_3O_{10}$ and Na-TSM were heated at 600 °C for 2.5 h and the particle sizes did not increase on either support. To further investigate kinetic effects, nanoparticles deposited on $KCa_2Nb_3O_{10}$ were heated *ex situ* at atmospheric pressure in pure hydrogen at 600 °C for 24 h and 48 h, and the average diameters of the nanoparticles were (4 ± 2) nm ($n$ = 116) and (4 ± 3) nm ($n$ = 192), respectively. It is believed the nanoparticles are reduced to elemental Rh during these experiments because XAS measurements (see below) of supported particles, reduced under less rigorous conditions, show a 90 % conversion of rhodium oxide to Rh by 500 °C.

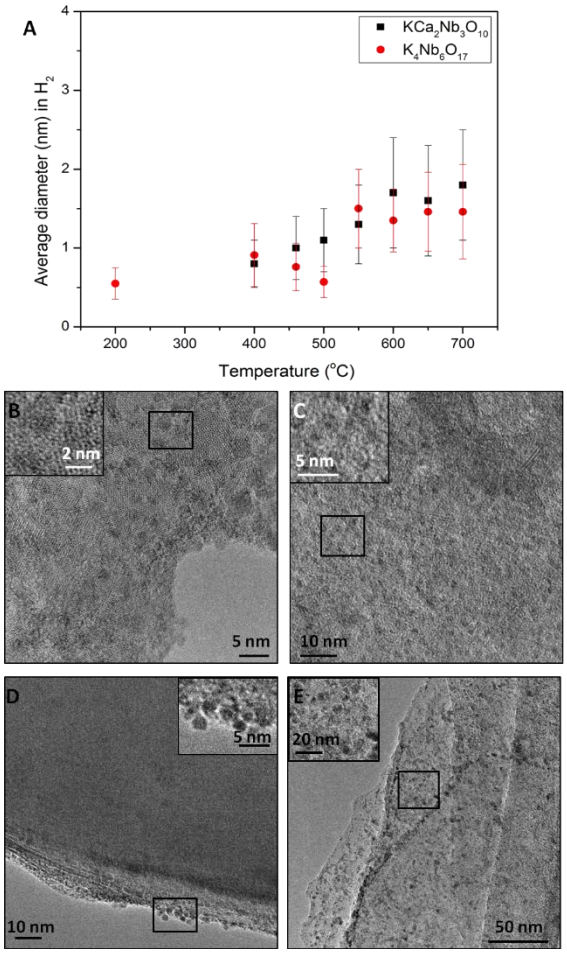


**Figure 4**. A) Plot of the average diameter of nanoparticles heated *in situ* in 200 Pa $H_2$ at increasing temperatures on $KCa_2Nb_3O_{10}$ and $K_4Nb_6O_{17}$. The uncertainty reported for each measured value is one standard deviation of the mean for $n$ measurements. See Supporting Information, Table S2 for number of measurements for each value. TEM images of nanoparticles on B) $KCa_2Nb_3O_{10}$ at 600 °C; C) $K_4Nb_6O_{17}$ at 600 °C; D) Na-TSM at 200 °C and E) Na-TSM at 600 °C.

As noted above, many previous studies of SMSI show evidence, especially from TEM and chemisorption data, that encapsulation of late transition metal nanoparticles occurs under reducing conditions.[18,19,22,23] With oxide nanosheet supports under the conditions investigated here, there was no evidence in HRTEM images of encapsulation of the nanoparticles. Thus it appears in the present case that the unusual stabilization of Rh nanoparticles arises from a covalent bonding interaction with the layered niobate

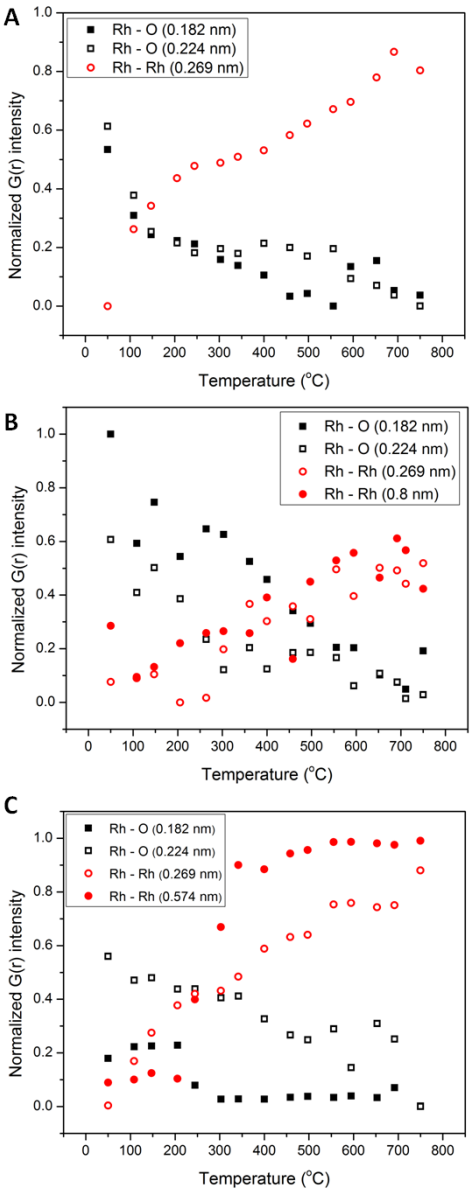


**Figure 5**. EXAFS spectra of rhodium catalyst on A) $KCa_2Nb_3O_{10}$ and B) Na-TSM heated *ex situ* in hydrogen for half an hour at each temperature. The spectra were taken at ambient conditions; C) Plot of Rh – Rh coordination number versus temperature for $KCa_2Nb_3O_{10}$ and Na-TSM shows the quicker reduction to rhodium metal nanoparticles on Na-TSM versus $KCa_2Nb_3O_{10}$. The errors are reported as one standard deviation of the mean for triplicate measurements.

supports. Rhodium oxide nanoparticles have previously been deposited on $SiO_2$, $CeZrO_2$, $ZrO_2$ and $CeO_2$ supports and heated in $H_2$ to reduce the particles. It was found that the activity of the catalyst for CO oxidation increased as $SiO_2 < ZrO_2 < CeZrO_2 < CeO_2$. It was suggested the activity increases in this manner because of the distribution of rhodium oxide on the support. This trend correlates with the d-electron acidity of the support, which increases in the order of increasing catalyst activity.[41] Another study showed zirconia retarded the growth of Pd nanoparticles, whereas $SiO_2$ and $\gamma$-$Al_2O_3$ supports did not have the same effect at 900 °C.[2,47] These trends are not easily explained by an SMSI model involving reduction of the support. Zirconia is not easily reduced nor does it suppress $H_2$ chemisorption, but it does maintain small particle sizes for late transition elements such as Rh and Pd.[2]

The transformation of supported $Rh(OH)_3$ to elemental Rh was studied using extended x-ray absorption spectroscopy (EXAFS). Samples were heated *ex situ* in hydrogen for 30 min at each temperature before x-ray absorption data were obtained under ambient conditions. Figure 5A-B shows the Fourier transform magnitude of the Rh - K edge EXAFS spectra for samples of $Rh(OH)_3$ deposited on $KCa_2Nb_3O_{10}$ and Na-TSM. The peak at 0.157 nm is due to Rh – O scattering, while the peak at 0.24 nm is due to Rh - Rh scattering. Figure 5A shows the Rh – Rh peak at 0.24 nm increasing slowly from 250 °C to 500 °C when the particles are deposited on $KCa_2Nb_3O_{10}$. This can be interpreted as a slow increase in rhodium particle size. At 500 °C, the magnitude of the peak at 0.24 nm is only 55 % of that of the rhodium foil. In contrast, for the Na-TSM support (Figure 5B), the peak magnitude at 0.24 nm is 80 % that of the rhodium foil. EXAFS spectra for $Rh(OH)_3$ and $Rh_2O_3$ were almost indistinguishable, and therefore $Rh_2O_3$ was used in the analysis although $Rh(OH)_3$ is present at room temperature. This could be the reason for the slight shift of the Rh – O peak, from 0.150 nm measured with the $Rh_2O_3$ standard, to 0.154 nm in the room temperature samples of $Rh(OH)_3$ on both supports. A plot of Rh – Rh coordination number versus temperature is shown in Figure 5C. Bulk rhodium metal has a coordination number of 12. The average

Rh – Rh coordination numbers of the nanoparticles deposited on $KCa_2Nb_3O_{10}$ and Na-TSM at 500 °C are 6 and 8, respectively. Coordination numbers smaller than 12 have previously been observed for fine Rh metal particles dispersed on supports.[48] Using the assumption the Rh particles are cuboctahedra, a coordination number of 9 correlates to approximately 3 nm diameter Rh metal particles.[48] This is in good agreement with the current study in which co ordination numbers of 6 and 8 correlate with particle diameters of $(1.1 \pm 0.4)$ nm and $(2.9 \pm 0.8)$ nm, respectively, as measured by TEM. However, it is important to note that the coordination number of Rh in bulk $Rh_2O_3$ is 6, and can be smaller in $Rh_2O_3$ nanoparticles. Thus, it is also possible that stabilization of $Rh_2O_3$ relative to Rh contributes to the lower coordination numbers observed on niobate supports. X-ray Absorption Near Edge Structure (XANES) analysis of samples reduced in 100 kPa $H_2$ indicates that Rh(III) is 80 % reduced to Rh(0) by 250 °C and 90 % by 500 °C on both $KCa_2Nb_3O_{10}$ and Na-TSM. While the rhodium is being reduced at the same rate for both supports, the coordination number increases more rapidly for the particles on Na-TSM than $KCa_2Nb_3O_{10}$. As noted above, the difference can be attributed to differences in the size of the precursor $Rh(OH)_3$ particles.

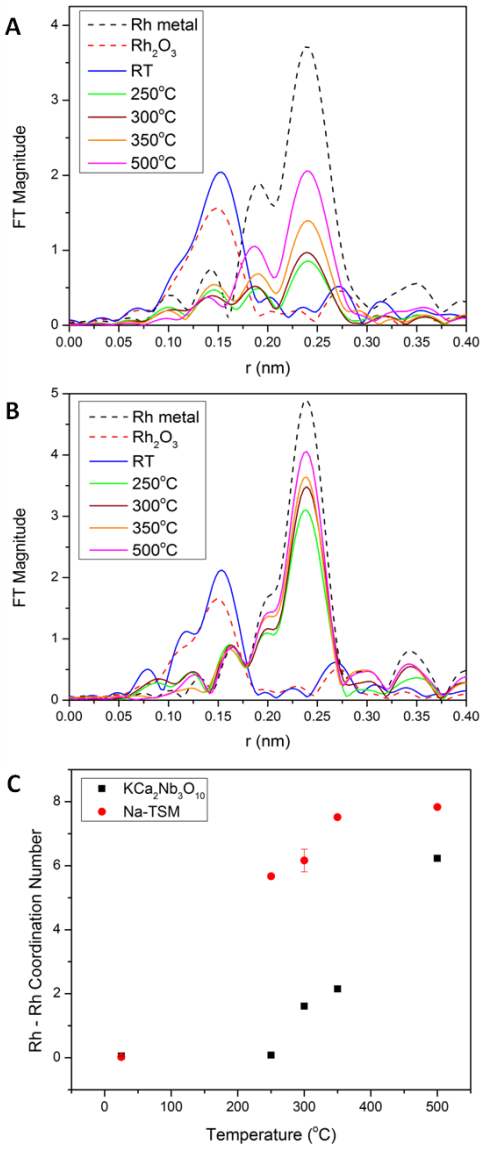


**Figure 6**. The normalized G(r) intensities for Rh–O and Rh-Rh correlations for rhodium hydroxide nanoparticles deposited on A) Na-TSM B) $KCa_2Nb_3O_{10}$ and C) $K_4Nb_6O_{17}$ upon heating in hydrogen.

High energy X-ray diffraction was performed and analyzed via pair-distribution functions (PDF) to track the rate of reduction of rhodium-oxygen bonds and growth of Rh metal nanoparticles deposited on the oxide supports in a reducing atmosphere. PDF data followed the same qualitative trends with data obtained from TEM and XAS. $Rh(OH)_3$ on $KCa_2Nb_3O_{10}$, $K_4Nb_6O_{17}$ and Na-TSM supports were heated *in situ* in 100 kPa hydrogen for the duration of the experiment. Figure 6A shows plots of normalized G(r) intensity versus temperature for rhodium – rhodium distances of 0.269 nm and rhodium – oxygen distances of 0.182 nm and 0.224 nm. The rhodium-rhodium distance correlates to the first shell bond length in rhodium metal and the rhodium - oxygen distances correlate to bond lengths in $Rh_2O_3$. These plots show the simultaneous decrease of Rh - O and increase of Rh - Rh bonding. Figure 6a shows a sharp decrease in normalized G(r) intensity at the Rh - O bond length and a sharp increase of Rh – Rh bonding for nanoparticles deposited on Na-TSM. Both of these curves begin to plateau around 250 °C. This is in agreement with XANES data that show > 80 % conversion from rhodium oxide to Rh at 250 °C for particles deposited on Na-TSM. On the other hand, with $KCa_2Nb_3O_{10}$ and $K_4Nb_6O_{17}$ nanosheets as supports, the decrease of Rh - O and increase of Rh – Rh normalized G(r) intensity is more gradual (Figure 6B-C). This suggests that the niobate supports stabilize $Rh_2O_3$ relative to Rh nanoparticles and thus postpones the reduction of Rh(III) to higher temperatures.

The diameters of Rh nanoparticles were determined by TEM statistical size analysis and correlate with the PDF analysis. TEM analysis shows that at 400 °C, the average size of nanoparticles deposited on $KCa_2Nb_3O_{10}$ and heated in hydrogen is 0.8 nm. In Figure 6b, the normalized G(r) intensity at 0.8 nm Rh-Rh distance has an inflection point at 400 °C, indicating an increase in nanoparticle diameter to 0.8 nm at this temperature. PDF analysis for nanoparticles deposited on $K_4Nb_6O_{17}$ also correlates to the TEM analysis. An Rh - Rh interatomic distance of 0.574 nm was investigated for this sample, as shown in Figure 5c. A sharp increase in the normalized G(r) intensity for this Rh - Rh distance occurs at 250 °C. TEM analysis shows the nanoparticle size is 0.55 nm at 200 °C and 0.9 nm at 400 °C. Therefore, the PDF estimate of particle diameter correlates well with the TEM statistical analysis.

## References


(1) Lee, T.; Liu, J.; Chen, N.-P.; Andres, R. P.; Janes, D. B.; Reifenberger, R. *J. Nanopart. Res.* **2000**, *2*, 345.
(2) Hansen, T. W.; DeLaRiva, A. T.; Challa, S. R.; Datye, A. K. *Acc. Chem. Res.* **2013**, *46*, 1720.
(3) Cao, A.; Lu, R.; Veser, G. *PCCP* **2010**, *12*, 13499.
(4) Hata, H.; Kobayashi, Y.; Bojan, V.; Youngblood, W. J.; Mallouk, T. E. *Nano Lett.* **2008**, *8*, 794.
(5) O'Hare, D.; Parker, K. H.; Winlove, C. P. *Med. Eng. Phys.* **2006**, *28*, 982.
(6) Cominos, V.; Hessel, V.; Hofmann, C.; Kolb, G.; Zapf, R.; Ziogas, A.; Delsman, E. R.; Schouten, J. C. *Catal. Today* **2005**, *110*, 140.
(7) Schubert, M. M.; Hackenberg, S.; van Veen, A. C.; Muhler, M.; Plzak, V.; Behm, R. J. *J. Catal.* **2001**, *197*, 113.
(8) Pestryakov, A. N.; Bogdanchikova, N. E.; Knop-Gericke, A. *Catal. Today* **2004**, *91–92*, 49.
(9) Recupero, V.; Pino, L.; Cordaro, M.; Vita, A.; Cipitì, F.; Laganà, M. *Fuel Process. Technol.* **2004**, *85*, 1445.
(10) Bartholomew, C. H. *Appl. Catal., A.* **1993**, *107*, 1.
(11) He, J.; Kunitake, T. *Chem. Mater.* **2004**, *16*, 2656.
(12) Wang, J.; Lu, A.-H.; Li, M.; Zhang, W.; Chen, Y.-S.; Tian, D.-X.; Li, W.-C. *ACS Nano* **2013**, *7*, 4902.
(13) Tauster, S. J. *Acc. Chem. Res.* **1987**, *20*, 389.
(14) Tauster, S. J.; Fung, S. C.; Baker, R. T. K.; Horsley, J. A. *Science* **1981**, *211*, 1121.
(15) Tauster, S. J.; Fung, S. C.; Garten, R. L. *J. Am. Chem. Soc.* **1978**, *100*, 170.
(16) Arjad, A. B.; Yarmoff, J. A. *J. Phys. Chem. C.* **2012**, *116*, 23377.
(17) Belzunegui, J. P.; Sanz, J.; Rojo, J. M. *J. Am. Chem. Soc.* **1990**, *112*, 4066.
(18) Bernal, S.; Botana, F. J.; Calvino, J. J.; Lopez, C.; Perez-Omil, J. A.; Rodriguez-Izquierdo, J. M. *J. Chem. Soc., Faraday Trans.* **1996**, *92*, 2799.
(19) Fu, Q.; Wagner, T.; Olliges, S.; Carstanjen, H.-D. *J. Phys. Chem. B.* **2004**, *109*, 944.
(20) Hu, Z.; Nakamura, H.; Kunimori, K.; Asano, H.; Uchijima, T. *J. Catal.* **1988**, *112*, 478.
(21) Martens, J. H. A.; Prins, R.; Zandbergen, H.; Koningsberger, D. C. *J. Phys. Chem.* **1988**, *92*, 1903.
(22) Silly, F.; Castell, M. R. *J. Phys. Chem. B.* **2005**, *109*, 12316.
(23) Liu, X.; Liu, M.-H.; Luo, Y.-C.; Mou, C.-Y.; Lin, S. D.; Cheng, H.; Chen, J.-M.; Lee, J.-F.; Lin, T.-S. *J. Am. Chem. Soc.* **2012**, *134*, 10251.
(24) Campbell, C. T. *Nat Chem* **2012**, *4*, 597.
(25) Jarvis, E. A.; Carter, E. A. *Phys. Rev. B.* **2002**, *66*, 100103.
(26) Brewer, L. *Acta Metall.* **1967**, *15*, 553.
(27) Srikrishnan, V.; Ficalora, P. J. *Metallurgical Transactions* **1974**, *5*, 1471.
(28) Ma, R.; Kobayashi, Y.; Youngblood, W. J.; Mallouk, T. E. *J. Mater. Chem.* **2008**, *18*, 5982.
(29) Campbell, C. T.; Starr, D. E. *J. Am. Chem. Soc.* **2002**, *124*, 9212.
(30) Farmer, J. A.; Campbell, C. T. *Science* **2010**, *329*, 933.
(31) Wiseman, T.; Williston, S.; Brandts, J. F.; Lin, L.-N. *Anal. Biochem.* **1989**, *179*, 131.
(32) Ghai, R.; Falconer, R. J.; Collins, B. M. *J. Mol. Recognit.* **2012**, *25*, 32.
(33) Dion, M.; Ganne, M.; Tournoux, M. *Mater. Res. Bull.* **1981**, *16*, 1429.
(34) Gasperin, M.; Le Bihan, M. T. *J. Solid State Chem.* **1982**, *43*, 346.
(35) Kobayashi, Y.; Hata, H.; Salama, M.; Mallouk, T. E. *Nano Lett.* **2007**, *7*, 2142.
(36) Fukuda, K.; Nakai, I.; Ebina, Y.; Ma, R.; Sasaki, T. *Inorg. Chem.* **2007**, *46*, 4787.
(37) Kaschak, D. M.; Johnson, S. A.; Hooks, D. E.; Kim, H.-N.; Ward, M. D.; Mallouk, T. E. *J. Am. Chem. Soc.* **1998**, *120*, 10887.
(38) Chen, Y.; Zhao, X.; Ma, H.; Ma, S.; Huang, G.; Makita, Y.; Bai, X.; Yang, X. *J. Solid State Chem.* **2008**, *181*, 1684.
(39) Hata, H.; Kobayashi, Y.; Mallouk, T. E. *Chem. Mater.* **2006**, *19*, 79.
(40) Fu, Q.; Yang, F.; Bao, X. *Acc. Chem. Res.* **2013**, *46*, 1692.
(41) Ligthart, D. A. J. M.; van Santen, R. A.; Hensen, E. J. M. *Angew. Chem. Int. Ed.* **2011**, *50*, 5306.
(42) Padeste, C.; Cant, N.; Trimm, D. *Catal. Lett.* **1994**, *28*, 301.
(43) Nagai, Y.; Hirabayashi, T.; Dohmae, K.; Takagi, N.; Minami, T.; Shinjoh, H.; Matsumoto, S. i. *J. Catal.* **2006**, *242*, 103.

(44) Shinjoh, H. *Catal Surv Asia* **2009**, *13*, 184.
(45) McCarty, J. G.; Malukhin, G.; Poojary, D. M.; Datye, A. K.; Xu, Q. *J. Phys. Chem. B.* **2004**, *109*, 2387.
(46) Biesterbos, J. W. M.; Hornstra, J. *J. Less Common. Met.* **1973**, *30*, 121.
(47) DeLaRiva, A. **2010**, *PhD Dissertation*, University of New Mexico.
(48) Ohyama, J.; Teramura, K.; Okuoka, S.-i.; Yamazoe, S.; Kato, K.; Shishido, T.; Tanaka, T. *Langmuir* **2010**, *26*, 13907.

## Charge Transfer Stabilization of Late Transition Metal Oxide Nanoparticles on a Layered Niobate Support

Late transition metal nanoparticles dispersed on high surface area oxide supports are essential to technologies in the energy, chemical, and environmental industries, where they are employed as catalysts and electrocatalysts. The activity and selectivity of these catalysts are dependent on the size[1-8] and shape[9] of the active nanoparticles, the composition of the oxide support,[1-5,10] and the extent of support reduction.[4,5,11-15] Therefore, the interfacial interactions between catalytic nanoparticles and supports are key parameters in determining catalyst stability, activity and selectivity. Under catalytic reaction conditions, nanoparticles can grow to form larger, less active particles. The rate and extent of particle growth is controlled in large measure by the details of the nanoparticle/support interface. Both theoretical[16-20] and experimental studies[4,21-25] have investigated the atomic-level structure of this interface. Although nanoparticle-support interactions are clearly implicated in the migration of particles leading to coalescence and in the kinetics of Ostwald ripening, there is still relatively little direct experimental quantification of the bonding at the nanoparticle-support interface.[4,26]

We reported the use of solution-based isothermal titration calorimetry (ITC) to quantify the heat of interaction between rhodium hydroxide nanoparticles and several early transition metal oxide and main group oxide supports.[26] These heats were also found to be strongly dependent on the oxide support composition. Stronger interfacial bonding was found to inhibit nanoparticle sintering in vacuum and under reducing atmospheres at elevated temperatures. Rhodium hydroxide nanoparticles bond exothermically to early transition metal (niobium, tantalum, and tungsten) oxide supports, which inhibit nanoparticle sintering. Conversely, the interfacial bonding to main group oxide supports, such as silica and alumina, is endothermic and particle growth on these oxides occurs at a much lower temperature.[26]

In the present study, we combine calorimetric measurements with density functional theory (DFT) calculations to map out the periodic trends in the strength of the nanoparticle-support interaction and to understand the reason for the anomalously strong bonding of late transition metals to early transition metal oxides. ITC was used to quantify the heats of interaction of cobalt, iridium, nickel, copper and silver metal oxide/hydroxide nanoparticles to a layered niobium oxide support and compared to a high surface area silicon oxide support. In situ high-resolution transmission electron microscopy (HRTEM) and high-angle annular dark field scanning transmission electron microscopy (HAADF STEM) were used to track the sintering of nanoparticles as a function of temperature under vacuum. A clear correlation between the strength of interfacial bonding and the resistance of nanoparticles to growth in vacuum was observed. DFT calculations of model systems were consistent with the experimental data and provided insight into the nature of charge transfer interactions that strongly stabilize late transition metal/metal oxide nanoparticles on early transition metal oxide supports.

**Nanoparticle deposition on layered oxide supports.** Nanosheets derived from the layer perovskite $KCa_2Nb_3O_{10}$, and the synthetic mica Na-TSM were used as model early transition metal oxide and main group oxide supports, respectively. As in our earlier study,[26] the use of these nanosheets enabled observation of nanoparticle growth on the crystallographically well-defined basal plane surface, and provided thin, electron-transparent samples for imaging of the nanoparticles by HRTEM and HAADF-STEM. The phase purity of $KCa_2Nb_3O_{10}$ and its acid-exchanged derivative $HCa_2Nb_3O_{10}\cdot 1.5\ H_2O$ were confirmed by comparing XRD patterns to literature reports.[28] $HCa_2Nb_3O_{10}\cdot 1.5\ H_2O$ was exfoliated into nanosheets of $TBA_{0.24}H_{0.76}Ca_2Nb_3O_{10}$ in excess aqueous $TBA^+OH^-$ solutions as described previously.[26,29]

Our earlier study quantified the heat of interfacial bonding between $Rh^{3+}$ hydroxide nanoparticles and oxide supports. To more broadly investigate periodic trends, the oxides/hydroxides of five additional late

transition metal ions ($Ir^{3+}$, $Co^{2+}$, $Ni^{2+}$, $Cu^{2+}$, $Ag^{+}$) were investigated. These ions were selected based on the solubility of their halide salts and, in all cases except $Ir^{3+}$, the rapid ligand exchange kinetics of the metal aquo ions. Metal oxide/hydroxide nanoparticles were deposited onto $TBA_{0.24}H_{0.76}Ca_2Nb_3O_{10}$ and Na-TSM nanosheets by *in situ* alkaline hydrolysis of the metal salt precursor, at a mass fraction of 0.05 metal. The same metal salts were used in ITC experiments to measure the interfacial bonding heats, as described below.

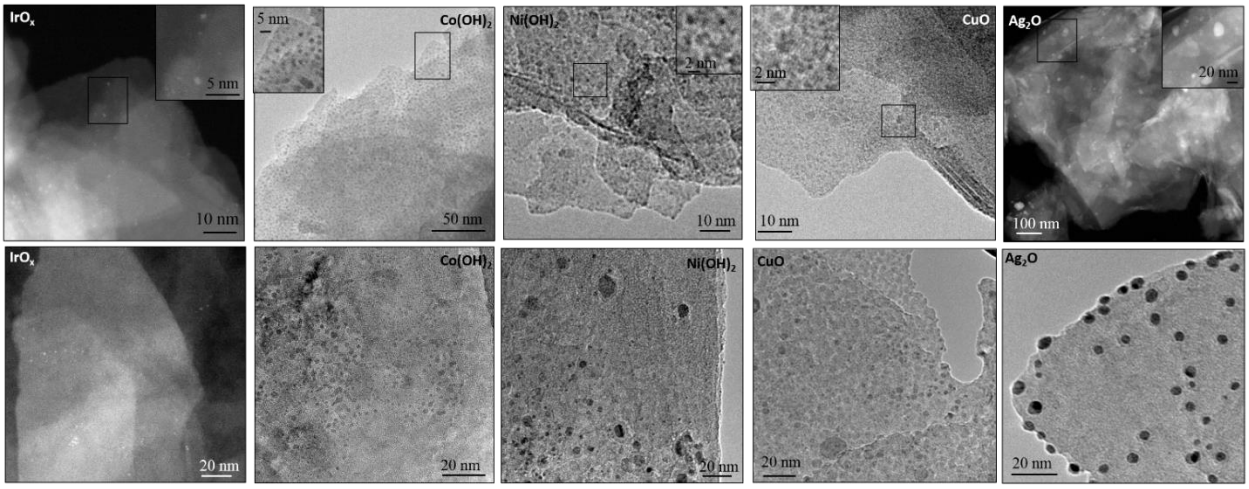


**Figure 1**. Ambient temperature HRTEM and HAADF STEM images of nanoparticles deposited at room temperature on $KCa_2Nb_3O_{10}$ (top) and Na-TSM (bottom).

The HRTEM and HAADF STEM images on the top row of Figure 1 illustrate the size distribution of hydroxyiridate-capped $IrO_x{\cdot}nH_2O$, $Co(OH)_2$, $Ni(OH)_2$, CuO, and $Ag_2O$ nanoparticles deposited onto $TBA_{0.24}H_{0.76}Ca_2Nb_3O_{10}$ nanosheets at ambient temperature, and Table 1 lists the deposited nanoparticle average diameter. Except in the case of $Ag_2O$, there is a spatially uniform distribution of nanoparticles on the niobate support. The average diameter of the $Ag_2O$ particles (7 nm) is much larger than the other deposited nanoparticles (1 nm -2 nm). For comparison purposes, the same nanoparticles were deposited onto the layered silicate Na-TSM. Na-TSM contains tetrahedral-octahedral-tetrahedral (T-O-T) silicate layers separated by $Na^+$ ions. Each tetrahedral layer is capped by oxygen atoms shared by two T atoms, and therefore there are no free Si-OH groups on the basal plane surface. The saturation loading of nanoparticles and their distribution onto Na-TSM was in stark contrast to nanoparticles deposited onto $KCa_2Nb_3O_{10}$, as shown in the bottom row of images in Figure 1. There was a broader size distribution of nanoparticles, as well as areas of the support with no nanoparticles present, and there were also large particles in the suspension, as seen in the TEM, that were not bound to the support in the case of both CuO and $Ag_2O$.

**Table 1**. Average nanoparticle diameter of metal oxide/hydroxide nanoparticles deposited onto nanosheets of $TBA_{0.24}H_{0.76}Ca_2Nb_3O_{10}$ and Na-TSM at room temperature as determined from TEM analysis. The number in parentheses represents the number of measurements used to determine one standard deviation of the mean.

| | $TBA_{0.24}H_{0.76}Ca_2Nb_3O_{10}$ | Na-TSM |
|---|---|---|
| Metal NP | Diameter (nm) (*n*) | Diameter (nm) (*n*) |
| $IrO_x{\cdot}nH_2O$ | 0.9 ± 0.2 (151) | 1.3 ± 0.5 (53) |
| $Co(OH)_2$ | 1.2 ± 0.5 (304) | 2.1 ± 0.5 (154) |

| | | |
|---|---|---|
| $Ni(OH)_2$ | 1.3 ± 0.4 (153) | 6 ± 3 (201) |
| CuO | 2.0 ± 0.6 (320) | 6 ± 5 (66) |
| $Ag_2O$ | 7 ± 5 (216) | 5 ± 2 (219) |

In our earlier study, micron-sized $Rh(OH)_3$ particles were found to break up and deposit as < 1 nm diameter particles on nanosheets of $TBA_{0.24}H_{0.76}Ca_2Nb_3O_{10}$.[26] This "reverse" ripening effect was attributed to the thermodynamically favorable interaction between $Rh(OH)_3$ and the oxide support, which overcomes the surface energy penalty of forming smaller particles. "Reverse" ripening experiments were performed on Co, Ni, Cu, and Ag oxide/hydroxide particles by hydrolyzing the metal halide precursors in $TBA^+OH^-$ for 18 h before their addition to a suspension of $TBA_{0.24}H_{0.76}Ca_2Nb_3O_{10}$ nanosheets in 25 mmol $L^{-1}$ $TBA^+OH^-$.

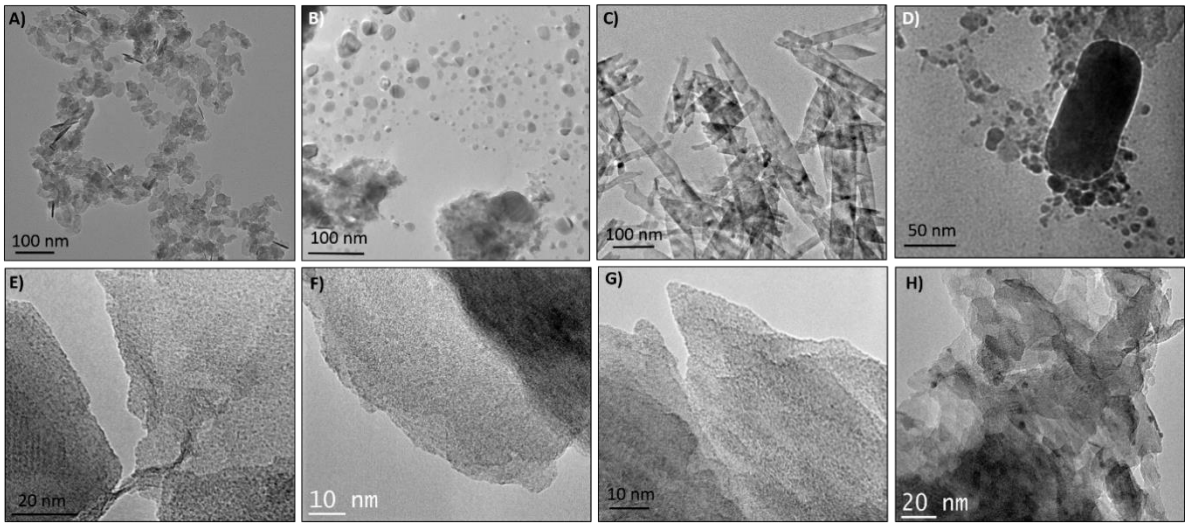


**Figure 2**. TEM images from "reverse" ripening experiments in which pre-formed particles were mixed with suspensions of $TBA_{0.24}H_{0.76}Ca_2Nb_3O_{10}$ nanosheets. Panels A – D show pre-formed particles of $Co(OH)_2$, $Ni(OH)_2$, CuO and $Ag_2O$, respectively. E – H show the nanoparticles derived from the same elements, respectively, after deposition onto the nanosheets.

In all cases, the deposited nanoparticles were smaller after addition of the nanosheet suspension, and in a few cases, the shape of the nanoparticles changed dramatically. For example, CuO particles formed in the absence of nanosheets were rods with an outer diameter of (19 ± 13) nm (n = 95), $Co(OH)_2$ particles were both thin platelets with an average lateral dimension of (22 ± 11) nm (n = 193) and rods, and $Ni(OH)_2$ particles were a mixture of spherical particles, platelets and wires (not all shapes are pictured in Figure 2b). Upon addition of the pre-formed metal oxide/hydroxide particles to colloidal $TBA_{0.24}H_{0.76}Ca_2Nb_3O_{10}$, all the metal oxides/hydroxides deposited as much smaller nanoparticles and no rod-shaped particles were found. Not all of the pre-formed $Co(OH)_2$ and $Ag_2O$ particles deposited on the nanosheets, and $Co(OH)_2$ particles deposited with a broad size distribution on different areas of the nanosheets. Figure 2 shows TEM images of the pre-formed nanoparticles (top) and their deposition onto $TBA_{0.24}H_{0.76}Ca_2Nb_3O_{10}$ nanosheets (bottom).

The interaction heats between metal oxide/hydroxide nanoparticles and oxide supports were measured by using ITC titrations as previously described.[26] The deposition of the nanoparticles onto an oxide support involves several chemical steps, and therefore, the enthalpy change that corresponds to the nanoparticle-

support interaction must be obtained by difference from the overall heat of reaction. Scheme 1 shows a generic Born-Haber cycle for the deposition of a metal oxide/hydroxide ($M(O/OH)_{(s)}$) from a metal halide precursor ($MX_{(aq)}$). The overall enthalpy change of the reaction ($\Delta H_4$) is the sum of the enthalpies of bonding ($\Delta H_3$), hydrolysis ($\Delta H_2$), and neutralization ($\Delta H_1$). This Born-Haber cycle was used for cobalt, nickel, copper and silver deposition. The enthalpy of neutralization ($\Delta H_1$= (-58 ± 2) kJ $mol^{-1}$) was included only in cases when hydrolysis of the metal salt precursor generated acid. The deposition of iridium oxide represents a special case, since we have recently found that colloidal solutions of ligand-free $IrO_x \cdot nH_2O$ nanoparticles prepared by alkaline hydrolysis of $[IrCl_6]^{2-}$ solutions contain strongly adsorbed hydroxyiridate ions $[Ir(OH)_5(H_2O)]^{2-}$ and $[Ir(OH)_6]^{2-}$.[32] ITC experiments were performed to measure the heats of adsorption of each individual component. First, the $IrO_x \cdot nH_2O$ colloidal solution was purified as previously reported to remove the monomeric anions from the surface of the nanoparticles.[32] Interestingly, there was no measurable heat of interaction between these purified particles and $TBA_{0.24}H_{0.76}Ca_2Nb_3O_{10}$ nanosheets. Next, the heat of interaction between the monomeric anions and nanosheets was measured and found to be -83 ± 17 kJ $mol^{-1}$. From these data, it could be concluded that only the monomeric anions are interacting with the support when $IrO_x \cdot nH_2O$ nanoparticles are deposited onto the nanosheets. Therefore, we use the interaction heat of the monomeric anions in plotting the periodic trends below (Figure 3). It should be noted that alkaline solutions of the monomer in equilibrium with air contain both $Ir^{III}$ and $Ir^{IV}$ forms of the monomer ($[Ir(OH)_5(H_2O)]^{2-}$ and $[Ir(OH)_6]^{2-}$, respectively), but EPR experiments show that the predominant form is $Ir^{III}$, [32] and therefore we refer to the equilibrium mixture of anions simply as $[Ir(OH)_5(H_2O)]^{2-}$.

**Scheme 1**. General Born-Haber cycle for metal oxide/hydroxide nanoparticle deposition onto oxide supports during ITC experiments.

(1) $HCl_{(aq)} + TBA^+OH^-_{(aq)} \rightarrow TBA^+Cl^-_{(aq)} + H_2O_{(l)}$ $\Delta H_1$

(2) $MX_{n(aq)} + nTBA^+OH^-_{(aq)} \rightarrow M(O/OH)_{n(s)} + nTBA^+X^-_{(aq)}$ $\Delta H_2$

(3) $M(O/OH)_{n(s)} + TBA^+/\ sheets^-_{(s)} \rightarrow M(O/OH)_n/TBA^+/sheets^-_{(s)}$ $\Delta H_3$

(4) $MX_{n(aq)} + (1+n)TBA^+OH^-_{(aq)} + HCl_{(aq)} + TBA^+/\ sheets^-_{(s)} \rightarrow$

$M(O/OH)_n/TBA^+/sheets^-_{(s)} + TBA^+Cl^-_{(aq)} + nTBA^+X^-_{(aq)} + H_2O_{(l)}$ $\Delta H_4$

Figure 3 shows the molar enthalpy of adsorption of the metal nanoparticles (or monomer in the case of $Ir^{III}$) to $TBA_{0.24}H_{0.76}Ca_2Nb_3O_{10}$ nanosheets, plotted against [$\Delta H_{sub}$ - $\Delta H_f$], the difference between the sublimation enthalpy of the bulk metal and the heat of formation of the most stable metal oxide (experimental values of $\Delta H_{sub}$ *and* $\Delta H_f$ used for each metal are provided in Table S2). This quantity represents the heat of forming the metal oxide from metal atoms and thus follows the trend in M-O bond energy. These enthalpy changes are plotted as kJ per mole of metal atoms. The $\Delta H_3$ values span a broad range, from quite exothermic to mildly endothermic. The strongest bonding to the niobate sheets is $[Ir(OH)_5(H_2O)]^{2-}$ with an interaction heat

of (-83 ± 17) kJ mol$^{-1}$, while the weakest is with $Ag_2O$ at (6 ± 7) kJ mol$^{-1}$. This endothermic heat of interaction can be measured since the enthalpy of the overall reaction is favorable; that is, reactions 1 and 2 drive the adsorption of nanoparticles to the support. The general trend is toward weaker interfacial bonding as the strength of the M-O bond in the bulk oxide decreases, as observed in earlier calorimetric studies of metal clusters binding to oxide supports,[5] although this is the first demonstration of this correlation for binding from a liquid-phase metal precursor solution. While the same trend is followed for metals on the silica support, in that case, the interaction energies are endothermic and there is less of a difference between elements with stronger and weaker M-O bonding.

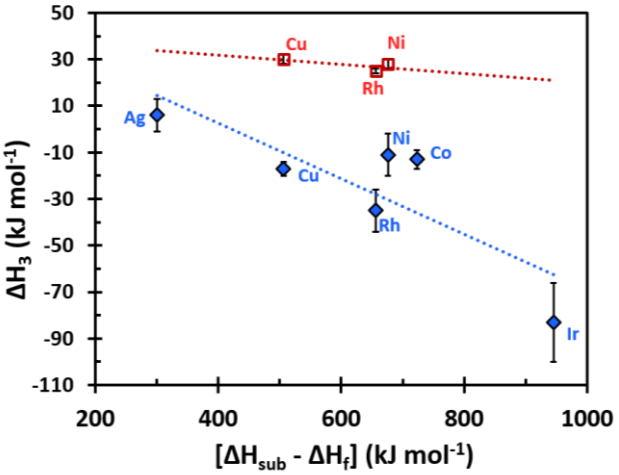


**Figure 3**. Thermochemical data for heats of interaction between metal oxide/hydroxide nanoparticles (or monomeric anions in the case of Ir) and supports for $TBA_{0.24}H_{0.76}Ca_2Nb_3O_{10}$ nanosheets (blue diamonds) and high surface area silica (red squares). The $SiO_2$ nanoparticle support had an average particle diameter of (17 ± 6) nm (n = 101) and a surface area of (408 ± 8) m$^2$ g$^{-1}$. Enthalpy changes are plotted per mole of transition metal M. The x-axis represents M-O bond strength as the difference between the heat of sublimation of the bulk metal and the heat of formation of its most stable oxide.

It is apparent from the comparison of Table 1 and Figures 2 and 3 that well-dispersed and smaller nanoparticles are grown on the niobate support as the heat of interaction becomes more exothermic. Upon deposition, $Rh(OH)_3$ nanoparticles on $TBA_{0.24}H_{0.76}Ca_2Nb_3O_{10}$ have an average diameter of less than 1 nm and a heat of interaction of (-35 ± 9) kJ mol$^{-1}$.[26] In contrast $Ag_2O$ has a slightly endothermic interaction heat (6 ± 7) kJ mol$^{-1}$ and deposits at room temperature as unevenly distributed particles with an average size diameter of (7 ± 5) nm. The broad distribution of particle sizes for the metal oxides studied on Na-TSM (Table 1) correlates with the endothermic interaction energy with the high surface area silica support. The resistance of supported nanoparticles to sintering follows a similar trend in which the thermodynamic driving force for particle growth is reduced by a strong bonding interaction of the nanoparticle with the support. Therefore, hydroxyiridate-capped $IrO_x{\cdot}nH_2O$ nanoparticles deposited on a niobium support are remarkably resistant to sintering at temperatures up to 1000 °C (Figure 4).

Campbell and co-workers have shown that metals that bond more strongly to oxygen also interact more exothermically with oxide supports.[5] In their experiments, like those described here, the composition of the support has a clear effect on the strength of this interaction.[5] "Strong" supports such as $CeO_2$ and $Fe_3O_4$ are differentiated from "weak" supports such as MgO by their more exothermic bonding to noble metal nanoparticles.[4,5] To better understand the nature of the interfacial interaction, the first set of DFT electronic structure calculations done in this work used a range of metals (Au, Ag, Cu, Pt, Pd, Ni, Ir, Rh, and Co) and models for representative oxide supports ($HCa_2Nb_3O_{10}$ and $SiO_2$). Because the extent of nanoparticle reduction in the experimental particle growth studies is unknown, and since previous experiments show similar trends for growth of $Rh(OH)_3$ nanoparticles when heated in vacuum and reducing atmospheres, we initially used fully reduced metal atoms and clusters to simplify the modeling. The calculations were then extended to metal atoms and clusters in higher oxidation states, which qualitatively show the same trends in bonding strength (see below). The calcium niobate nanosheets were modeled in their proton-exchanged form ($HCa_2Nb_3O_{10}$) by first optimizing the bulk structure, beginning with the experimentally characterized P4/*mbm* crystal structure refined by Chen *et al.*[29] The DFT-optimized bulk lattice constants were $a = b =$

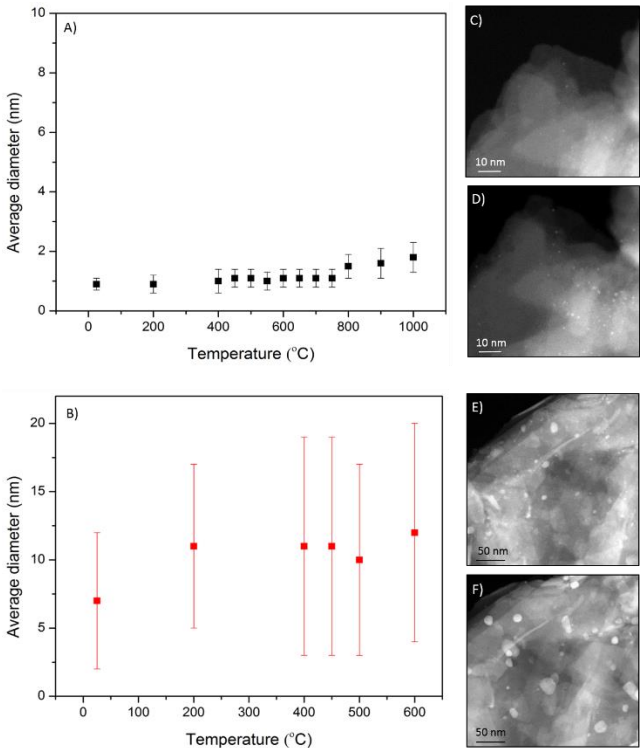


**Figure 4**. Plots of the average particle diameter of A) hydroxyiridate-capped $IrO_x \cdot nH_2O$ and B) $Ag_2O$ deposited on $TBA_{0.24}H_{0.76}Ca_2Nb_3O_{10}$ nanosheets, after restacking with KOH. The uncertainty in each measurement is reported as one standard deviation of the mean for *n* measurements. (Supporting information, Table S3). HAADF STEM images of hydroxyiridate-capped $IrO_x \cdot nH_2O$ supported on $KCa_2Nb_3O_{10}$ at C) 25 °C and D) 700 °C. E) and F) are HAADF STEM images of $Ag_2O$ on $KCa_2Nb_3O_{10}$ at 25 °C and 700 °C, respectively.

0.534 nm and $c$ = 1.464 nm, in reasonable agreement with the experimental values of $a = b$ = 0.545 nm and $c$ = 1.441 nm. From the optimized computed structure, the surface of the layered oxide was cleaved in the [001] direction, which is the layering axis of the crystal. $H_2O$ molecules that occupy the interlayer galleries in the bulk structure were not included in the computational model. The $SiO_2$ support was modeled using a reconstructed, partially hydroxylated β-cristobalite $SiO_2$(001) surface structure reported by Rozanska *et al.*, which is predicted to be stable under the conditions employed in this study and is commonly used to model amorphous silica supports.[41]

Binding energies for both single metal atoms and four-atom tetrahedral clusters (denoted $M_4$) were calculated to model metal-oxide support interaction strengths. Binding energies were calculated relative to the clean oxide surface plus a gas phase metal atom (or cluster): $E_{bind} = E_{metal/support} - E_{support\text{-}[clean]} - E_{metal\text{-}[g]}$, where $E_{metal\text{-}[g]}$ is the energy of the gas phase metal atom (or cluster), $E_{support\text{-}[clean]}$ is the energy of the clean support surface, and $E_{metal/support}$ is the energy of the metal-adsorbed surface. Negative values indicate exothermic binding.

For single atoms, structural optimization calculations were initiated from three possible surface binding sites on the $HCa_2Nb_3O_{10}$ surface: (1) the equatorial oxygen, (2) the axial oxygen, or (3) the interstitial space between $NbO_6$ polyhedra. The optimized structure of Ir and Ag atoms are shown in Figure 5A and 5B, respectively, and demonstrate that the equatorial oxygen site is preferred for Ir, which interacts strongly, whereas the interstitial site is preferred for Ag, which interacts more weakly. In both cases, there is a resulting close contact between the adsorbed metal and niobium atoms in the support. For Ir and Ag, the optimized metal-niobium internuclear distances are 0.27 nm and 0.31 nm, respectively. This suggests that metal-metal bonding between the adsorbed metal and the underlying niobium atom is indeed possible. The optimized structure of all the metal atoms studied on $HCa_2Nb_3O_{10}$ are shown in Figure S8, where similar metal-metal distances (Table S4) were observed, except for Au, which preferred the axial oxygen binding site. The optimized single atom metal adsorption site for $SiO_2$ binding is the same for all metals.

The optimized $M_4$ adsorption structures for Ir and Ag on $HCa_2Nb_3O_{10}$ are provided in Figure 5C and 5D, respectively. Both of these metallic clusters prefer the interstitial bonding site with a 3-atom basal plane in contact with surface oxygen atoms, although $Ag_4$ sits flat above the surface. The optimized $M_4$ adsorption structures for all the metals demonstrate that all metals (except Au) prefer the interstitial site with the 3-atom basal plane in contact with the surface. In Figure 6A-B, the resulting binding energies are plotted against [$\Delta H_{sub}$ - $\Delta H_f$] for each metal. A linear correlation between the oxide formation energy and the metal-support binding strength emerges from the calculations. The niobate and silicate supports are strong and weak, respectively, as also shown in the experimental data in Figure 3.

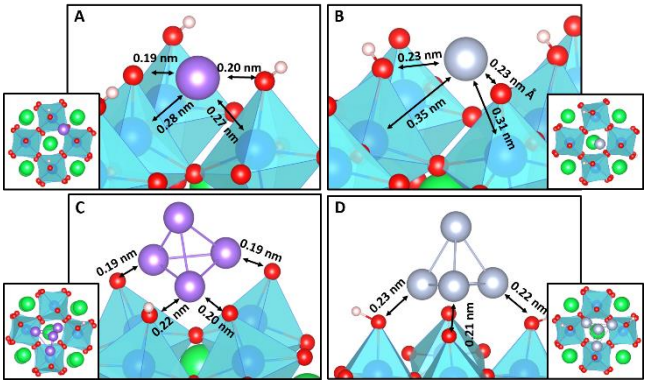


**Figure 5**. Optimized adsorption geometries and internuclear distances on $HCa_2Nb_3O_{10}$ for single atoms of (A) Ir and (B) Ag and for $M_4$ clusters of (C) Ir and (D) Ag.

This type of correlation was first proposed and experimentally demonstrated by Campbell and Sellers[5] and can serve as a useful computational screening tool for selecting candidates for supported catalytic metals with specific interaction strengths. The plots in Figure 6 demonstrate that platinum-group metals bind strongly to the niobate support, whereas late transition metals interact weakly with the silica support. The resulting periodic trend in interaction strength across late transition metal atoms and clusters is in agreement with the experimental trend in adsorption strengths of metal oxides ($\Delta H_3$) determined by ITC and shown in Figure 3. The DFT calculations are also consistent with the experimental observation that the composition of the support strongly affects the interfacial bonding enthalpy. All metal nanoparticles investigated interact weakly with the $SiO_2$ support, as shown experimentally in Figure 3 and computationally in Figure 6.

The effect of the oxidation state of the metal atom was then investigated for comparison with the experimentally measured heats of interaction determined by ITC. The binding energies of all metals were calculated on an

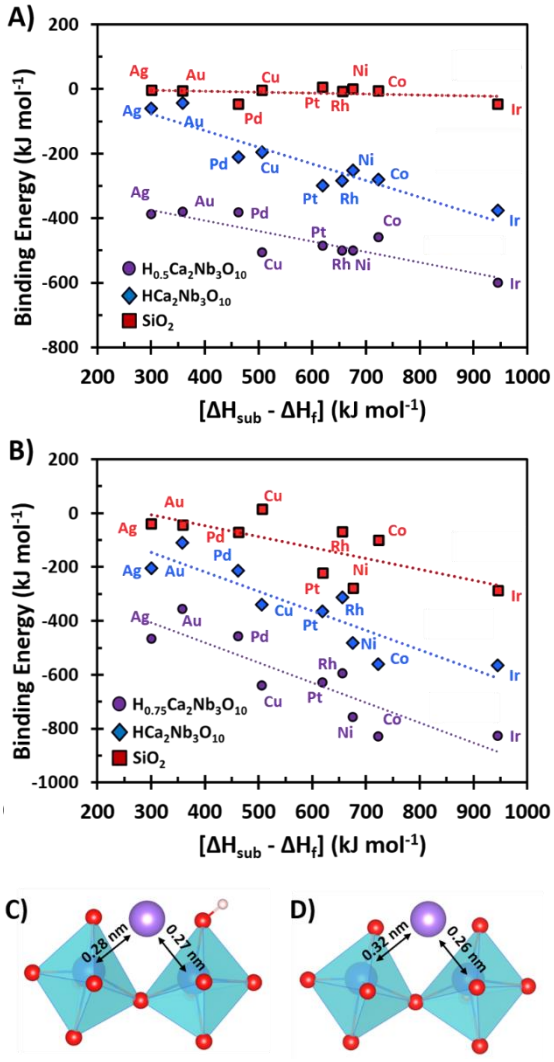


**Figure 6**. Binding energies for (A) single metal atoms and (B) $M_4$ metal clusters on niobium oxide and silica surfaces plotted against the formation enthalpy of the corresponding metal's most stable oxide calculated relative to a single gas phase metal atom, [$\Delta H_{sub} - \Delta H_f$]. Structural interfaces of iridium adsorbed to (C) stoichiometric and (D) non-stoichiometric niobium oxide surfaces.

$H_{0.5}Ca_2Nb_3O_{10}$ surface model, which changed the formal oxidation state of the metal from $M^0$ to $M^{1+}$. This yields an oxidation state equivalent to adsorbing a metal atom with an attached –OH group (and desorbing $H_2O$ in the adsorption process). The data in Figure 6A show stronger adsorption to the $H_{0.5}Ca_2Nb_3O_{10}$ surface than to the stoichiometric surface, and the same qualitative trend in bonding strength is obtained regardless of the oxidation state of the metal. Figure 6C-D compares the structural interface models of iridium calculated in different oxidation states. The Ir-Nb bond distance is decreased over the $H_{0.5}Ca_2Nb_3O_{10}$ surface, reflecting stronger binding induced by the Ir-Nb interaction. The good correlation between theory and experiment suggests that the periodic trends in nanoparticle/support interactions are insensitive to the metal oxidation state, as observed experimentally in the Rh/$Rh(OH)_3$ case.[26] This suggests that DFT modeling can be used to investigate a broader range of metals than might be experimentally accessible for ITC thermodynamic analysis.

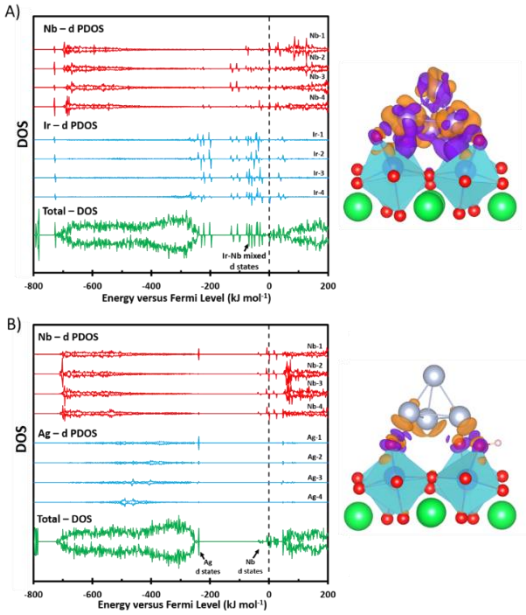


**Figure 7**. Total and partial density of states plotted relative to the Fermi level for $HCa_2Nb_3O_{10}$ supported (A) Ir and (B) Ag 4-atom clusters. The total DOS is shown in green, the PDOS projected on the d-states of the Nb surface atom adjacent to the adsorbed metal atom is shown in red, and PDOS projected on the d-states of the adsorbed metal atom is shown in blue. Spin up and spin down states are plotted on the positive and negative axes, respectively. The Fermi level is denoted by the vertical dotted line. Charge density difference isosurfaces are shown on the right, where the purple regions reflect negative charge accumulation and the orange regions reflect charge depletion. The accumulation and depletion isosurfaces are shown at values of ± 0.4 $e$ $nm^{-1}$.

Analysis of metal-support electronic structures provides insight into the nature of the metal-oxide support bonding. The difference in bonding character between Ir and Ag on the niobium oxide is demonstrated by the density of states (DOS) analysis shown in Figure 7. In Figure 7A, there is clear mixing of Ir and Nb d-states, indicative of electron transfer from Ir atoms to the nearest adjacent niobium atoms in the support. This suggests some degree of metal-metal bonding and is further confirmed by the Bader charge differences (calculated as the Bader charge of the surface-bound metal atom relative to the valence of the gas phase metal atom) reported in Table S6. A pronounced negative charge depletion on the surface-bound Ir atom is observed. The isostructural plots in Figure 7 show the charge density difference calculated between the full metal-support system and the clean-support/metal-atom components, revealing how charge is transferred between the cluster and the support. For the iridium cluster, there is significant valence electron density between Ir and Nb at the interface demonstrated by the purple isosurface, which again suggest a strong Ir-Nb bonding interaction. Conversely, no mixing of d-states between Ag and niobium is seen in the DOS plots in Figure 7B, resulting in a high energy gap state relative to the d-band and weak Ag binding. Correspondingly, there is no valence electron density accumulation between the cluster and support in the Ag system seen in the charge density difference. This conclusion is also consistent for the bonding between the niobium support and single metal atoms demonstrating that the results are not dependent on the chosen cluster model.

The Bader charge analysis for $HCa_2Nb_3O_{10}$ demonstrates that for all metals tested there is significant *negative charge transfer* from the transition metal atom to the niobate support, whereas there is little charge

transfer to or from the transition metal to $SiO_2$. In fact, for Ir and Ni on $SiO_2$, there is actually a small amount of charge transfer *from* the support to the adsorbed metal; this is also reflected in the charge density difference plot for Ir-$SiO_2$. The role of d-orbital mixing in stabilizing bimetallic transition metal alloys and interfaces has a long history in the experimental and theoretical literature. Brewer proposed in 1967 that d-acid/base interactions between early and late transition metals, respectively, could account for the anomalous stability of alloys such as $ZrPt_3$.[42] Later electronic structure calculations by Wang and Carter, however, showed that in these alloys charge transfer occurred in the opposite direction, from the early to the late transition metal.[43] Strong evidence for electron transfer in the Brewer sense (from the more to the less electronegative metal) has been found for ultrathin films of late transition metals such as Pd, Ni, and Cu on earlier transition metal (Mo, W, Ru) surfaces.[44-47] In these studies, Goodman concluded that the electronegativity of the surface atoms was lower than those in the bulk metal.[45] The present results suggests that the Brewer d-acid/base interaction is quite relevant to the interaction of transition metal and metal oxide nanoparticles with "strong" supports, which have empty or partially filled d-orbitals. A key factor appears to be the coincidence of d-orbital energies in the relevant oxidation states of the two metals, as shown for $Ir^0$ and $Nb^{5+}$ in Fig. 7A. It is interesting to note that Ag binds weakly to the niobate support because the d-orbitals of Ag are significantly lower in energy than those of $Nb^{5+}$. As demonstrated in Figures 3 and 6, metals that form stronger M-O bonds are also observed to bind stronger to the oxide support. Our electronic structure analysis, however, suggests that electron donation from the adsorbed metal atom occurs mainly to the Nb on the layered niobate structures, suggesting that the supported metal atoms oxidation tendencies can be predictive of strong support interactions independent from the destination of charge transferred upon adsorption. This suggests the possibility of tuning the strength of the metal-support interactions for late transition metals through appropriate choice of d-electron accepting oxide supports. Experiments along these lines are currently underway

## References


(1) Goodman, D. W. *Chem. Rev.* **1995**, *95*, 523.
(2) Haruta, M. *Catal. Today* **1997**, *36*, 153.
(3) Shekhar, M.; Wang, J.; Lee, W.-S.; Williams, W. D.; Kim, S. M.; Stach, E. A.; Miller, J. T.; Delgass, W. N.; Ribeiro, F. H. *J. Am. Chem. Soc.* **2012**, *134*, 4700.
(4) Campbell, C. T. *Acc. Chem. Res.* **2013**, *46*, 1712.
(5) Campbell, C. T.; Sellers, J. R. V. *Faraday Discuss.* **2013**, *162*, 9.
(6) Cargnello, M.; Doan-Nguyen, V. V. T.; Gordon, T. R.; Diaz, R. E.; Stach, E. A.; Gorte, R. J.; Fornasiero, P.; Murray, C. B. *Science* **2013**, *341*, 771.
(7) Valden, M.; Lai, X.; Goodman, D. W. *Science* **1998**, *281*, 1647.
(8) Vayssilov, G. N.; Lykhach, Y.; Migani, A.; Staudt, T.; Petrova, G. P.; Tsud, N.; Skála, T.; Bruix, A.; Illas, F.; Prince, K. C.; Matolı´n, V. r.; Neyman, K. M.; Libuda, J. *Nat Mater* **2011**, *10*, 310.
(9) Mostafa, S.; Behafarid, F.; Croy, J. R.; Ono, L. K.; Li, L.; Yang, J. C.; Frenkel, A. I.; Cuenya, B. R. *J. Am. Chem. Soc.* **2010**, *132*, 15714.
(10) Haruta, M. *CATTECH* **2002**, *6*, 102.
(11) Bonanni, S.; Aït-Mansour, K.; Harbich, W.; Brune, H. *J. Am. Chem. Soc.* **2012**, *134*, 3445.
(12) Hu, Z.; Nakamura, H.; Kunimori, K.; Asano, H.; Uchijima, T. *J. Catal.* **1988**, *112*, 478.
(13) Tauster, S. J. *Acc. Chem. Res.* **1987**, *20*, 389.
(14) Tauster, S. J.; Fung, S. C.; Baker, R. T. K.; Horsley, J. A. *Science* **1981**, *211*, 1121.
(15) Wang, Y.-G.; Yoon, Y.; Glezakou, V.-A.; Li, J.; Rousseau, R. *J. Am. Chem. Soc.* **2013**, *135*, 10673.
(16) Meyer, R.; Ge, Q.; Lockemeyer, J.; Yeates, R.; Lemanski, M.; Reinalda, D.; Neurock, M. *Surface Science* **2007**, *601*, 134.
(17) Addou, R.; Senftle, T. P.; O'Connor, N.; Janik, M. J.; van Duin, A. C. T.; Batzill, M. *ACS Nano* **2014**, *8*, 6321.
(18) Negreiros, F. R.; Fabris, S. *The Journal of Physical Chemistry C* **2014**, *118*, 21014.
(19) Vilhelmsen, L. B.; Hammer, B. *Physical Review Letters* **2012**, *108*, 126101.
(20) Bruix, A.; Lykhach, Y.; Matolínová, I.; Neitzel, A.; Skála, T.; Tsud, N.; Vorokhta, M.; Stetsovych, V.; Ševčíková, K.; Mysliveček, J.; Fiala, R.; Václavů, M.; Prince, K. C.; Bruyère, S.; Potin, V.; Illas, F.; Matolín, V.; Libuda, J.; Neyman, K. M. *Angewandte Chemie International Edition* **2014**, *53*, 10525.
(21) Hansen, T. W.; DeLaRiva, A. T.; Challa, S. R.; Datye, A. K. *Accounts of Chemical Research* **2013**, *46*, 1720.
(22) Fu, Q.; Yang, F.; Bao, X. *Acc. Chem. Res.* **2013**, *46*, 1692.

(23) Hansen, P. L.; Wagner, J. B.; Helveg, S.; Rostrup-Nielsen, J. R.; Clausen, B. S.; Topsøe, H. *Science* **2002**, *295*, 2053.
(24) Campbell, C. T.; Parker, S. C.; Starr, D. E. *Science* **2002**, *298*, 811.
(25) Prieto, G.; Zečević, J.; Friedrich, H.; de Jong, K. P.; de Jongh, P. E. *Nat Mater* **2013**, *12*, 34.
(26) Strayer, M. E.; Binz, J. M.; Tanase, M.; Kamali Shahri, S. M.; Sharma, R.; Rioux, R. M.; Mallouk, T. E. *J. Am. Chem. Soc.* **2014**, *136*, 5687.
(27) Stuckless, J. T.; Frei, N. A.; Campbell, C. T. *Rev. Sci. Instrum.* **1998**, *69*, 2427.
(28) Dion, M.; Ganne, M.; Tournoux, M. *Mater. Res. Bull.* **1981**, *16*, 1429.
(29) Chen, Y.; Zhao, X.; Ma, H.; Ma, S.; Huang, G.; Makita, Y.; Bai, X.; Yang, X. *J. Solid State Chem.* **2008**, *181*, 1684.
(30) Hata, H.; Kobayashi, Y.; Bojan, V.; Youngblood, W. J.; Mallouk, T. E. *Nano Lett.* **2008**, *8*, 794.
(31) Ma, R.; Kobayashi, Y.; Youngblood, W. J.; Mallouk, T. E. *J. Mater. Chem.* **2008**, *18*, 5982.
(32) Zhao, Y.; Vargas-Barbosa, N. M.; Strayer, M. E.; McCool, N.; Pandelia, M.-E.; Saunders, T.; Swierk, J.; Callejas, J.; Jensen, L.; Mallouk, T. E. *J. Am. Chem. Soc.* **2015**, *137*, 9.
(33) Kresse, G.; Furthmuller, J. *Comput. Mater. Sci.* **1996**, *6*, 15.
(34) Kresse, G.; Furthmuller, J. *Phys. Rev. B* **1996**, *54*, 11169.
(35) Perdew, J. P.; Chevary, J. A.; Vosko, S. H.; Jackson, K. A.; Pederson, M. R.; Singh, D. J.; Fiolhais, C. *Phys. Rev. B* **1992**, *46*, 6671.
(36) Kresse, G.; Joubert, D. *Phys. Rev. B* **1999**, *59*, 1758.
(37) Monkhorst, H. J.; Pack, J. D. *Phys. Rev. B* **1976**, *13*, 5188 LP
(38) Bader, R. F. W. *Accounts of Chemical Research* **1985**, *18*, 9.
(39) Henkelman, G.; Arnaldsson, A.; Jonsson, H. *Comput. Mater. Sci.* **2006**, *36*, 354.
(40) Zhao, Y.; Hernandez-Pagan, E. A.; Vargas-Barbosa, N. M.; Dysart, J. L.; Mallouk, T. E. *The Journal of Physical Chemistry Letters* **2011**, *2*, 402.
(41) Rozanska, X.; Delbecq, F.; Sautet, P. *Physical Chemistry Chemical Physics* **2010**, *12*, 14930.
(42) Brewer, L. *Acta Metall.* **1967**, *15*, 553.
(43) Wang, H.; Carter, E. A. *J. Am. Chem. Soc.* **1993**, *115*, 2357.
(44) Campbell, R. A.; Rodriguez, J. A.; Goodman, D. W. *Surface Science* **1990**, *240*, 71.
(45) Rodriguez, J. A.; Campbell, R. A.; Goodman, D. W. *Journal of Physical Chemistry* **1991**, *95*, 5716.
(46) Rodriguez, J. A.; Goodman, D. W. *Journal of Physical Chemistry* **1991**, *95*, 4196.
(47) Heitzinger, J. M.; Gebhard, S. C.; Koel, B. E. *Surface Science* **1992**, *275*, 209.

## Critical role of water in generating highly active and selective supported Au catalysts for CO preferential oxidation for hydrogen purification

Preferential oxidation of CO (PROX) has the potential for economically purifying the over 9 Billion tons of commercially produced $H_2$ in the US. Using a $Au/Al_2O_3$ catalyst, we show that CO levels can be readily reduced to < 10 ppm with minimal $H_2$ loss and no catalyst deactivation over 9 hours. The catalyst can be operated at space velocities 1-2 orders of magnitude higher than most literature reports, dramatically increasing $H_2$ throughput. The key to obtaining high activity and selectivity lies in carefully controlling both the space velocity feed water content. Results are consistent with a recently proposed CO oxidation mechanism as well as previous PROX kinetics studies, and indicate that the CO and $H_2$ oxidation reactions are largely sequential. Operating the catalyst in an optimum window of support water coverage with appropriate space velocities maximizes selectivity by controlling the number of active sites available for $H_2$ oxidation.

The chemical industry produces over 9 Billion tons of hydrogen for several important processes, including ammonia synthesis (primarily for fertilizer production), petroleum refining, and hydrogenation reactions [1,2]. Hydrogen is generally produced from light hydrocarbons via steam reforming and water gas shift reactions. The resulting reformate typically contains about 1% CO in $H_2$; this CO must be removed for many downstream applications, particularly hydrogen destined for fuel cells. State-of-the-art Pt-Ru fuel cell anode catalysts require CO levels below 50 ppm; lower levels may allow for the use of simpler monometallic materials [3]. Economically removing the last 1% CO impurity has proved challenging. Pressure swing adsorption (PSA) requires large capital investments and low flow rates, which reduces throughput and limits $H_2$ recovery to 70-90% [2]. Methanation ($CO + 3H_2 \rightarrow CH_4 + H_2O$) uses ~5% of the produced $H_2$, but actual $H_2$ losses are typically 10-15% due to the unselective methanation of $CO_2$ present in the reformate [2].

Another option is the preferential oxidation (PROX) reaction of CO with $O_2$, which requires highly selective catalysts to limit $H_2$ consumption. The often-stated goal for this reaction is to reduce the CO concentration to 50 ppm ("CO slip") with $O_2$ selectivity to $CO_2 \geq 50\%$; we will refer to this as the 50/50 goal. Supported Au nanoparticles are now well known to be highly active CO oxidation catalysts [4-6] but notoriously poor hydrogenation catalysts [7]. They should be excellent PROX catalysts, but 20 years of research has produced very few catalysts capable of achieving the 50/50 goal (Fig. 1A) [8,9]. Numerous studies have searched for better catalysts, examining particle size effects [6,10], metal oxide support effects [11,12], mixed metal oxides [10,13], and ordered mesoporous materials [14]. Bimetallic catalysts [15], the inclusion of polyoxometallates in a liquid phase reaction scheme [16], Au-ceria nanocomposites [17], and embedded $Au@CeO_2$ catalysts [18] have also been examined with limited success in achieving the 50/50 goal.

Mechanistic PROX investigations have shown that $H_2$ promotes CO oxidation over Au [19] and the metal-support interface plays a critical role in the catalysis [5,19-21]. A general lack of consensus on the mechanism of CO oxidation, however, has severely hampered catalyst development. A newly proposed mechanism indicates water plays the critical mechanistic role of a co-catalyst during CO oxidation over $Au/TiO_2$ catalysts [5]. Preliminary tests showed $Au/Al_2O_3$ catalysts were more selective for PROX, yet have the same basic CO oxidation reaction kinetics, and thus likely the same mechanism. Although the promotional effects of water in PROX have been reported [9,22], there is no systematic study seeking to control activity and selectivity by adjusting the feed water content. We therefore studied a commercial $Au/Al_2O_3$ catalyst, adding water to a model reformate gas. To readily compare catalyst performance, we defined a simple figure of merit:

$$FOM = \frac{O_2\ selectivity\ (\%)}{CO\ slip\ (ppm)} \qquad (1)$$

For reference, a FOM value of 1 describes a catalyst and reaction conditions that meet the 50/50 goal. Several FOM values are plotted against the nominal activity for some of our experimental conditions in Fig 1A. Approximately 60 literature reports are included, most of which were collected at 80°C, the operating temperature of many fuel cell systems [3]. The literature results vary greatly, so nominal activities are normalized to the total amount of Au; no adjustments for Au particle size were made. We are aware of only two reports that achieve the 50/50 goal, both using low space velocities and nominally dry feeds [8,9]. By controlling the amount of water added to the reaction (*vide infra*) and using higher space velocities, we far surpass the 50/50 goal, and do so at space velocities that are 1-2 orders of magnitude larger than literature reports (Fig. 1A).

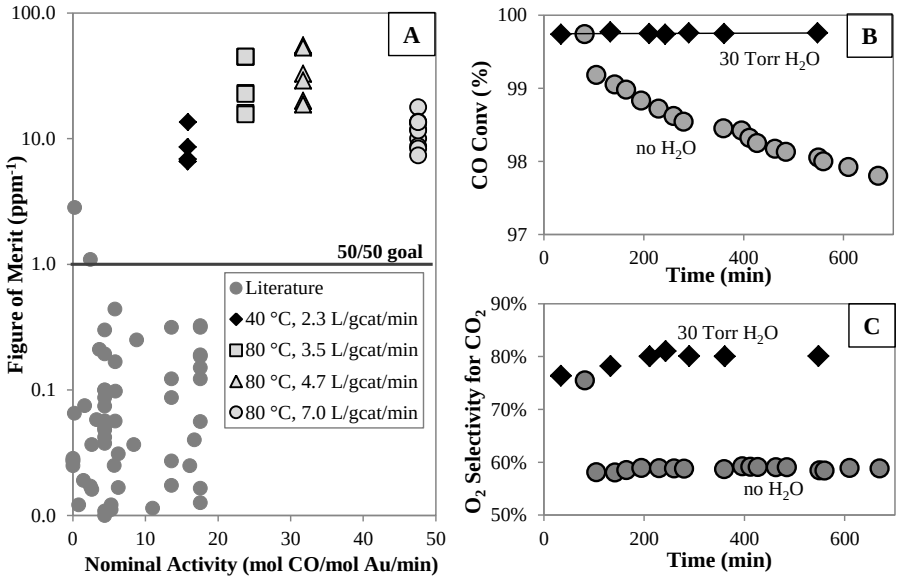


**Figure 1.** PROX performance and deactivation of $Au/Al_2O_3$ with water in the feed (1% CO, 1.4% $O_2$, 60% $H_2$, bal He). (A) Performance comparison between $Au/Al_2O_3$ with added water (ca. 1-20 Torr, see Fig. 2) and literature reports. (B) CO conversion and (C) $O_2$ selectivity during 9 hour experiments with $Au/Al_2O_3$ at 80 °C.

Catalyst longevity is similarly important in PROX, and water may prevent carbonates deposition, which poison CO oxidation [23-25]. Long term activity and selectivity plots are shown in Figs. 1B and 1C, respectively. When water is added to the feed, there is no deactivation over the course of 9 hours, and $O_2$ selectivity remains both constant and high. When water is removed, $O_2$ selectivity immediately drops and the CO oxidation activity begins to degrade over time. These experiments, which employ an unoptimized catalyst, show that huge leaps in PROX performance are possible when the feed water content is carefully controlled. The potential hydrogen production per unit time is increased 1-2 orders of magnitude over previous reports, with little to no catalyst deactivation.

Figure 2 shows details for the PROX experiments in Fig. 1A. The experimental protocol was critical to achieve high activity and selectivity, so catalysts were always equilibrated with 30 Torr water before initiating the reaction. The water pressure ($P_{H2O}$) was then systematically lowered, allowing the CO conversion to stabilize at each $P_{H2O}$ (generally 30 min). Figures 2B and 2C show that optimizing the space velocity (SV) is critical to achieving high activity and selectivity. When both $P_{H2O}$ and SV are properly controlled, the reaction can operate at very high conversions (99.9%, < 10 ppm CO slip) while maintaining high $O_2$ selectivity (> 80%); if the SV drops too low, $O_2$ selectivity suffers (Fig. 2C).

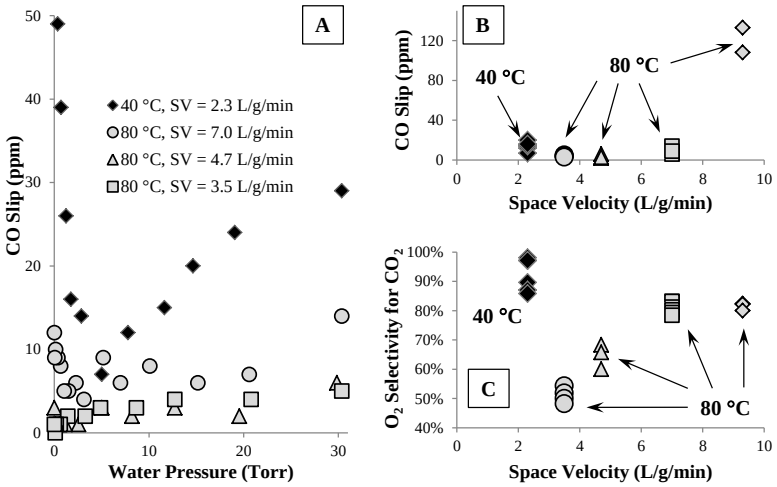


**Figure 2.** PROX reactivity over $Au/Al_2O_3$ at high conversions. (A) CO slip vs. $P_{H2O}$; (B) CO slip vs. space velocity; and (C) $O_2$ selectivity vs. space velocity. CO slip ≡ concentration of CO in the reactor outlet; SV units are $L/g_{cat}/min$.

A space velocity study at 20°C (Figs. 3A and 3B) demonstrated CO conversion increases as the SV decreases while $O_2$ selectivity is essentially the same up to 99% CO conversion. Similarly, when CO conversions are high (CO slip ~ 10 ppm), decreasing the SV only serves to decrease the $O_2$ selectivity (Figs. 2B and 2C; 80°C). These data indicate the PROX reaction is largely sequential, with CO reacting before $H_2$. This conclusion differs somewhat from the most popular literature mechanisms, which either require $H_2$ activation to generate the active oxidant [26], or utilize support O atoms [19].

The trends in PROX activity and selectivity, both for our data and much of the PROX literature, can be readily understood in the context of our recently proposed mechanism for CO oxidation over $Au/TiO_2$ catalysts. The key elements of this mechanism are (i) the generation of reactive Au-OOH from $O_2$ and a proton from water adsorbed at the metal-support interface, (ii) a very low reaction barrier between Au-OOH and Au-CO, and (iii) rate limiting decomposition of Au-COOH [5]. The CO oxidation kinetics and H/D kinetic isotope effect for $Au/Al_2O_3$ are nearly identical to $Au/TiO_2$, indicating the same mechanism is likely at work. Our results are largely consistent with the extensive PROX mechanistic work from the Behm [19,24] and Piccolo [26] labs; however, there are two important distinctions from their interpretations. First, $H_2$ activation is not required for CO oxidation activity since the active Au-OOH species is derived from $O_2$ and water. Second, our mechanism does not require support O, making it consistent with isotope labeling studies in the absence of $H_2$ [27,28].

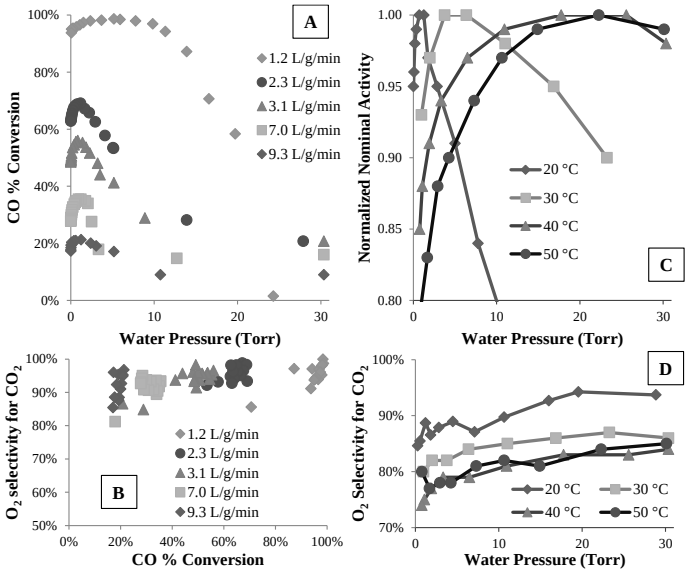


**Figure 3.** Effects of water on CO PROX catalysis over $Au/Al_2O_3$. (A) CO conversion and (B) $O_2$ selectivity for $CO_2$ at 20°C as a function of feed water and SV; (C) Normalized nominal activity and (D) $O_2$ selectivity for $CO_2$ as a function of $P_{H2O}$ and temperature.

Our results show that an un-optimized catalyst can be a commercially viable $H_2$ purification catalyst provided the SV, $\theta_{H2O}$, and reaction temperature are carefully controlled. Understanding the fundamental steps in the reaction mechanism essentially turn this from a catalyst optimization problem to one of reaction

engineering. Controlling SV and $\theta_{H2O}$ essentially allow one to tune the number of available active sites, allowing adjustments for differing feeds. This is a substantial advantage, potentially allowing one to uncover additional active sites as a catalyst begins to deactivate over time. For wet feeds, this may be accomplished simply by cooling to a temperature where the water vapor pressure is close to the $P_{H2O}$ required for maximum catalytic activity.

This is not to say that the catalyst cannot or should not be optimized; rather, the mechanistic understanding provides similarly clear directions to how the catalyst can be improved or tuned for specific conditions. Balancing the water binding properties of the support with the feed water content is likely to be important. Supports that bind water more tightly will be desirable for relatively dry feeds – this should reduce the need for adding water to the system; conversely, supports that bind water weakly will likely be better for wet feeds. Selectivity improvements should arise from tuning the CO and $H_2$ binding properties of Au, as Bond suggested [7]. Any electronic effects (e.g. support effects, particle size effects, or promoters) that increase CO adsorption energies greater than $H_2$ adsorption energies should provide for greater differentiation between the two reactants, and higher selectivity. Work is in progress to explore these potential effects on the activity and selectivity of PROX catalysts.

## References


1. H. J. Neef, *Energy* **34**, 327 (2009).
2. K. Liu, C. Song, V. Subramani, *Hydrogen and Syngas Production and Purification Technologies*. (John Wiley & Sons, Inc., 2010).
3. A. F. Ghenciu, in *Fuel Cells Compendium*, N. Brandon, D. Thompsett, Eds. (Elsevier, Oxford, UK, 2005), pp. 91-106.
4. I. X. Green, W. Tang, M. Neurock, J. T. Yates, Jr., *Science* **333**, 736 (2011).
5. J. Saavedra, H. A. Doan, C. J. Pursell, L. C. Grabow, B. D. Chandler, *Science* **345**, 1599 (2014).
6. M. Valden, X. Lai, D. W. Goodman, *Science* **281**, 1647 (1998).
7. G. C. Bond, C. Louis, D. T. Thompson, *Catalysis by Gold* G. J. Hutchings, Ed., Catalytic Science Series (Imperial College Press, London, 2006), vol. 6, pp. 366.
8. G. Avgouropoulos *et al.*, *Catal. Today* **75**, 157 (2002).
9. P. Landon *et al.*, *J. Mater. Chem.* **16**, 199 (2006).
10. R. J. H. Grisel, B. E. Nieuwenhuys, *J. Catal.* **199**, 48 (2001).
11. S. Ivanova, V. Pitchon, C. Petit, V. Caps, *ChemCatChem* **2**, 556 (2010).
12. D. Widmann, Y. Liu, F. Schueth, R. J. Behm, *J. Catal.* **276**, 292 (2010).
13. A. Tompos *et al.*, *J. Catal.* **266**, 207 (2009).
14. Y. Liu *et al.*, *J. Catal.* **296**, 65 (2012).
15. X. Li *et al.*, *ACS Catal.* **2**, 360 (2012).
16. W. B. Kim, T. Voitl, G. J. Rodriguez-Rivera, S. T. Evans, J. A. Dumesic, *Angew. Chem., Int. Ed.* **44**, 778 (2005).
17. S. Carrettin, P. Concepcion, A. Corma, J. M. Lopez Nieto, V. F. Puntes, *Angew. Chem., Int. Ed.* **43**, 2538 (2004).
18. M. Cargnello *et al.*, *Chem. Mater.* **22**, 4335 (2010).
19. D. Widmann, E. Hocking, R. J. Behm, *J. Catal.* **317**, 272 (2014).
20. T. Fujitani, I. Nakamura, T. Akita, M. Okumura, M. Haruta, *Angewandte Chemie International Edition* **48**, 9515 (2009).
21. M. Cargnello *et al.*, *Science* **341**, 771 (2013).
22. M. M. Schubert, A. Venugopal, M. J. Kahlich, V. Plzak, R. J. Behm, *J. Catal.* **222**, 32 (2004).
23. J. Saavedra, C. Powell, B. Panthi, C. J. Pursell, B. D. Chandler, *J. Catal.* **307**, 37 (2013).
24. B. Schumacher, Y. Denkwitz, V. Plzak, M. Kinne, R. J. Behm, *J. Catal.* **224**, 449 (2004).
25. Y. Denkwitz *et al.*, *J. Catal.* **251**, 363 (2007).
26. E. Quinet *et al.*, *J. Catal.* **268**, 384 (2009).
27. M. Ojeda, B.-Z. Zhan, E. Iglesia,. *J. Catal.* **285**, 92 (2012).
28. J. T. Calla, R. J. Davis, *J. Catal.* **241**, 407 (2006).

**Thiol Adsorption on Supported Au Nanoparticle Catalysts to Evaluate Au Dispersion and the Number of Actives Sites for Alcohol Oxidation Reactions**

***Background***. Supported Au catalysts show exceptional activity and/or selectivity at low temperatures in CO oxidation,[29,30] selective hydrogenations,[30,31] oxidations,[30,32,33] reductive coupling of nitroaromatics,[34] and the water-gas shift (WGS) reaction.[30,35] Several factors have been suggested for the exceptionally high activity of Au catalysts, including quantum size effects,[6] particle geometry,[36,37] under-coordinated Au atoms,[38-41] and the role of the metal-support interface.[29] In spite of the substantial research activity in gold catalyzed oxidation reactions, the factors controlling catalytic activity are still not well understood.

The number of active sites is a critical measurement in heterogeneous catalysis. Transmission electron microscopy (TEM) provides important information on particle size and an estimate of the fraction of surface atoms; however it struggles to detect the smallest metal nanoparticles and does not directly probe the number of active sites on a catalyst surface. Chemisorption is a desirable method because it provides a direct measure of the number of adsorption sites, samples a much larger number of particles and, in many cases, can also be used to estimate particle size. There have been a few attempts to develop adsorption methods using low temperature volumetric CO chemisorption[42-44] and methyl mercaptan adsorption monitored with gravimetry.[45] However, the reversible adsorption of CO on both Au and surface hydroxyl groups make it difficult to differentiate chemisorption on Au from physisorption on the support, so no widely accepted chemisorption method exists for supported Au catalysts.

Although improved chemisorption techniques would benefit the quantification of Au catalysis, chemisorption data may not necessarily correlate with the number of active sites for a specific reaction. An alternate method for evaluating the number of active sites on a catalyst is through intentional poisoning or titration experiments. In these experiments, a controlled amount of poison is added to a catalyst and the resulting reduction in activity is monitored. Changes in the catalytic activity as a function of the amount of added poison may therefore shed light on both the number of active sites and any distribution in the inherent reactivity of the active sites. This general method has been applied to acid-catalyzed reactions over zeolites, using substituted pyridines[46,47] or Na vapor[48,49] as the active site titrant. Fewer controlled poisoning studies have been applied to metal based catalysts. Turkevich and co-workers developed a pulse poison/titration experiment using a variety of poisons to study ethylene hydrogenation over supported Pt catalysts in the 1970s.[50] More recently, Finke and coworkers evaluated the number of catalytic active sites on a 5% $Rh/Al_2O_3$ catalyst using $CS_2$ poisoning experiments.[51]

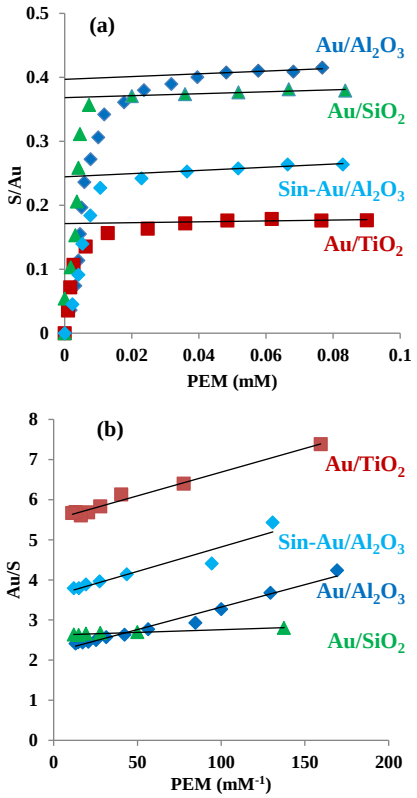


**Figure 1**. (a) Adsorption isotherms and (b) Langmuir plots for PEM adsorption on supported Au catalysts.

The seminal work by Bain and co-workers showed thiols form self-assembled monolayers (SAMs) on gold surfaces.[25] This rich surface chemistry has been extensively studied and expanded,[26] and led to the discovery that small gold nanoparticles could be prepared by reducing Au salts in the presence of thiols (the well-known Brust synthesis).[27] In this study, we sought to exploit Au-thiol chemistry to better understand the catalytic chemistry of Au. Specifically, we explored thiol adsorption as a method for evaluating the number of surface Au atoms in supported Au nanoparticle

catalysts. We further extended this investigation to develop controlled thiol poisoning to estimate the number of active sites on several Au catalysts during 4-methoxybenzyl alcohol oxidation. The combination of these tests, along with appropriate characterization studies, allow for a more complete description of the substantial differences in activity from one catalyst to the next.

***Results.*** Using the PEM molar absorptivity and the titration plots (data not shown) to determine the equilibrium concentration of thiol in solution at each point, it is also possible to present the data as a traditional adsorption isotherm (Figure 1a). Each of these methods can be used to determine an endpoint for the titration; as Table 1 shows, for a given catalyst, the three methods give essentially the same result. In the following discussion, we prefer to use the Langmuir plot since it uses the data points that have the smallest intrinsic experimental errors and extrapolates to a maximum adsorption value. The Langmuir plot also yields a value for the adsorption equilibrium constant at the end of the titration, which allows for comparisons between catalysts.

**Table 1**. PEM adsorption at 22 °C on the series of supported Au catalysts used in this study.

| Catalyst | Au wt % | Titration plot | S/Au (mole %) Extrapolated to [PEM] = 0 | Langmuir plot | $K_{eq}$ ($M^{-1}$) $\times 10^5$ | $\Delta G_{ads}$ (kJ/mol) |
|---|---|---|---|---|---|---|
| $Au/TiO_2$ | 0.88 | 19 ± 1 | 17 ± 1 | 18 ± 1 | 4.7 ± 0.2 | -32 ± 1 |
| $Au/Al_2O_3$ | 0.81 | 42 ± 1 | 40 ± 1 | 45 ± 1 | 2.0 ± 0.1 | -30 ± 1 |
| sin-$Au/Al_2O_3$ | 0.81 | 27 ± 1 | 25 ± 1 | 28 ± 1 | 3.0 ± 0.4 | -31 ± 1 |
| $Au/SiO_2$ | 1.21 | 39 ± 1 | 37 ± 1 | 38 ± 1 | 20 ± 2 | -36 ± 1 |

These studies also provide insight into the interactions between S and Au in SAMs and thiol MPCs, because the Au NPs are stabilized against agglomeration through strong bonds with the oxide support. Thus, the remaining surface is exposed and devoid of capping agents which may impact measurements associated with S-Au interactions. In particular, the nature of the Au-S bonding has been of debate, particular the oxidation states of the two species and the fate of the proton. To address this, and to evaluate how adsorbed thiols might change Au surface chemistry, we performed XPS studies, specifically looking for changes to Au oxidation state due to thiol adsorption. Figure 2 shows the Au 4f region for the $Au/TiO_2$ catalyst with and without adsorbed thiols. Thiol adsorption induces a slight Au core electron shift towards weaker binding energy, consistent with increased electron density on the Au. This suggests that thiol adsorption is, on balance, an electron donating interaction – there is no indication of Au oxidation.

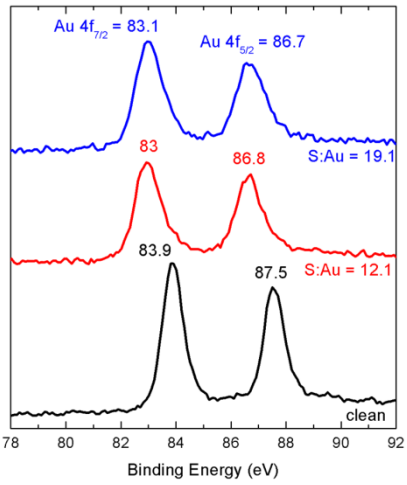


**Figure 2.** Au 4f spectra of clean and 1-butanethiol covered $Au/TiO_2$ catalysts. Spectra are offset for clarity.

Figure 3 shows the results from a series of kinetic titration experiments using 1-butanethiol to poison the $Au/Al_2O_3$ catalyst. Each data point in the figure is the result of a separate poisoning experiment in which the initial reaction rate was determined. The plot shows two clear regions. At low thiol concentrations (blue data points), the rate decreases linearly with added thiol. After adding about 10% thiol (relative to total Au), the data deviates from this trend (maroon data points); additional thiol becomes a less effective poison. This tailing effect was consistently observed for all of the catalysts using several different thiols, and has been observed in kinetic poisoning studies of different systems. Regardless of the origins of the tailing at higher thiol concentrations, it was consistently present and should be accounted for in using

the poisoning data. We chose to use the extrapolation of the linear poisoning regime (blue data in Figure 3) to the *x*-intercept as a metric related to the number of active sites. The value might be most appropriately interpreted as an estimate of the number of high activity sites.

In developing this technique as a method for evaluating the number of catalytic sites, we had two additional concerns: (i) the thiol chain length and steric crowding on the Au surface might affect the extrapolated value and (ii) competition between the thiol and the substrate (4-methylbenzyl alcohol, the concentration of which is orders of magnitude higher than the thiol) might influence the poisoning. We addressed these issues by (i) varying the thiol chain length and (ii) changing the point in the experiment in which thiols were introduced to the system. These experiments are compiled in Figure 4. In the first set of experiments (Figure 4a), we varied the thiol chain length, adding the thiol at the beginning of the experiment, before the substrate was added. This allowed the thiol to fully adsorb to the catalyst before substrate was introduced.

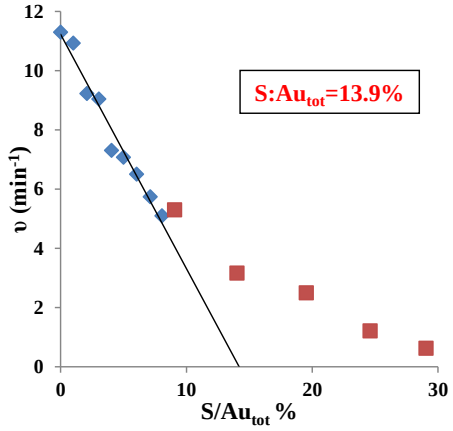


**Figure 3**. Au/$Al_2O_3$ activity for 4-methoxybenzyl alcohol oxidation in the presence of varying amounts of 1-butanethiol.

We also examined adding the thiol simultaneously with the substrate by initiating the reaction by adding the catalyst (Fig. 4b). Two noteworthy conclusions can be drawn from this data. First, under these conditions, there is a clear trend in poisoning effectiveness with chain length. Second, the *x*-intercepts of the plots in Figure 5b are shifted to larger S:$Au_{tot}$ values, indicating greater amounts of thiol are required to poison the most active sites on the catalyst. This was true for all of the thiols tested (see Fig. 4c). This suggests the substrate and thiols do indeed compete for active sites under these conditions, with longer chain thiols being less able to access the Au active sites. This is somewhat surprising, as one would not expect the order of addition to substantially affect the thermodynamics and competition for Au active sites. We note that all of these poisoning titration values are well within the strong adsorption regime of the UV-Vis studies. This suggests that the difference between the two types of thiol addition experiments is probing a subtle aspect of the reaction mechanism, not differences in thiol binding strength.

UV-Vis spectroscopy was used to follow phenethyl mecaptan (PEM) adsorption from hexane solution, thus providing a means for evaluating the total amount of surface Au available. Test Au/$Al_2O_3$ and Au/$TiO_2$ catalysts showed very similar behavior in PEM titrations, having essentially the same thiol binding constants and surface stoichiometry ($Au_{surf}$:S) of ~2. In spite of having a significantly higher surface thiol coverage ($Au_{surf}$:S ~1), the Au/$SiO_2$ catalyst had a somewhat stronger thiol binding constant.

We also developed a method for evaluating the number of benzyl alcohol oxidation active sites by intentionally adding small amounts of thiol to the reaction mixture. For all the

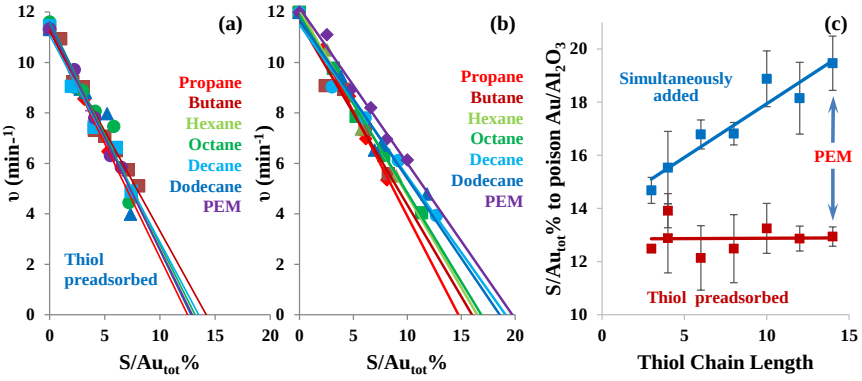


**Figure 4**. Effects of thiol chain length and order of addition on for 4-methoxybenzyl alcohol oxidation catalyzed by Au/$Al_2O_3$

thiols and catalysts tested, catalytic activity initially decreased linearly with thiol addition, but then tailed off. Extrapolating the linear portion of the plot to zero activity represents the best method for estimating the number of active sites on the catalyst.

Kinetic poisoning studies showed the $Au/TiO_2$ and $Au/Al_2O_3$ catalysts had a similar active site concentration. Interestingly, sintering the $Au/Al_2O_3$ catalyst, which had particles too small to observe by TEM, had only a small effect on the number of active sites. Correcting the catalytic activity of the catalysts for the number of thiol titration sites provided clear evidence that the support has a strong influence on the catalytic activity of Au in benzyl alcohol oxidation.

## References


(1) Saavedra, J.; Doan, H.; Pursell, C. J.; Grabow, L. C.; Chandler, B. D. *Science* **2014**, *in press*
(2) Takei, T.; Akita, T.; Nakamura, I.; Fujitani, T.; Okumura, M.; Okazaki, K.; Huang, J.; Ishida, T.; Haruta, M. *Adv. Catal.* **2012**, *55*, 1
(3) Corma, A.; Serna, P. *Science* **2006**, *313*, 332
(4) Zope, B. N.; Hibbitts, D. D.; Neurock, M.; Davis, R. J. *Science* **2010**, *330*, 74
(5) DellaPina, C.; Falletta, E.; Rossi, M. *Chem. Soc. Rev.* **2012**, *41*, 350
(6) Grirrane, A.; Corma, A.; Garcia, H. *Science* **2008**, *322*, 1661
(7) Shekhar, M.; Wang, J.; Lee, W.-S.; Williams, W. D.; Kim, S. M.; Stach, E. A.; Miller, J. T.; Delgass, W. N.; Ribeiro, F. H. *J. Am. Chem. Soc.* **2012**, *134*, 4700
(8) Valden, M.; Lai, X.; Goodman, D. W. *Science* **1998**, *281*, 1647
(9) Herzing, A. A.; Kiely, C. J.; Carley, A. F.; Landon, P.; Hutchings, G. J. *Science* **2008**, *321*, 1331
(10) Chen, M. S.; Goodman, D. W. *Science* **2004**, *306*, 252
(11) Falsig, H.; Hvolbæk, B.; Kristensen, I. S.; Jiang, T.; Bligaard, T.; Christensen, C. H.; Nørskov, J. K. *Angew. Chem., Int. Ed.* **2008**, *47*, 4835
(12) Lemire, C.; Meyer, R.; Shaikhutdinov, S.; Freund, H.-J. *Angew. Chem., Int. Ed.* **2004**, *43*, 118
(13) Lopez, N.; Janssens, T. V. W.; Clausen, B. S.; Xu, Y.; Mavrikakis, M.; Bligaard, T.; Norskov, J. K. *J. Catal.* **2004**, *223* (14) Mills, G.; Gordon, M. S.; Metiu, H. *J. Chem. Phys.* **2003**, *118*, 4198
(15) Oxford, S. M.; Henao, J. D.; Yang, J. H.; Kung, M. C.; Kung, H. H. *Applied Catalysis, A: General* **2008**, *339*, 180
(16) Menegazzo, F.; Manzoli, M.; Chiorino, A.; Boccuzzi, F.; Tabakova, T.; Signoretto, M.; Pinna, F.; Pernicone, N. *Journal of Catalysis* **2006**, *237*, 431
(17) Menegazzo, F.; Pinna, F.; Signoretto, M.; Trevisan, V.; Boccuzzi, F.; Chiorino, A.; Manzoli, M. *Applied Catalysis A: General* **2009**, *356*, 31
(18) van Vegten, N.; Haider, P.; Maciejewski, M.; Krumeich, F.; Baiker, A. *J. Colloid Interface Sci.* **2009**, *339*, 310
(19) Borgna, A.; Sepulveda, J.; Magni, S. I.; Apesteguia, C. R. *Appl. Catal., A* **2004**, *276*, 207
(20) Park, S. H.; Rhee, H. K. *Appl. Catal., A* **2001**, *219*, 99
(21) Coughlan, B.; Keane, M. A. *J. Catal.* **1992**, *138*, 164
(22) Simon, M. W.; Efstathiou, A. M.; Bennett, C. O.; Suib, S. L. *J. Catal.* **1992**, *138*, 1
(23) Gonzalez-Tejuca, L.; Aika, K.; Namba, S.; Turkevich, J. *J. Phys. Chem.* **1977**, *81*, 1399
(24) Brust, M.; Walker, M.; Bethell, D.; Schiffrin, D. J.; Whyman, R. *J. Chem. Soc. Chem. Commun.* **1994**, 801
(25) Boisselier, E.; Astruc, D. *Chemical Society Reviews* **2009**, *38*, 1759; (26) Daniel, M.-C.; Astruc, D. *Chemical Reviews* **2004**, *104*, 293.